



1 **Global zonal wind variations and responses to solar activity, and**
2 **QBO, ENSO during 2002–2019**

3 Xiao Liu^{1, 2}, Jiyao Xu^{2, 3}, Jia Yue^{4, 5}, and Vania F. Andrioli^{2, 6}

4 ¹Institute of Electromagnetic Wave, School of Physics, Henan Normal University, Xinxiang, 453000, China

5 ²State Key Laboratory of Space Weather, National Space Science Center, Chinese Academy of Sciences, Beijing, 100190,
6 China

7 ³University of the Chinese Academy of Science, Beijing, 100049, China

8 ⁴Physics Department, Catholic University of America, Washington, DC 20064, USA

9 ⁵NASA Goddard Space Flight Center, Greenbelt, MD, 20771, USA

10 ⁶Heliophysics, Planetary Science and Astronomy Division, National Institute for Space Research (INPE), Sao Jose dos
11 Campos, Sao Paulo, Brazil

12

13 *Correspondence to:* Jiyao Xu (xujy@nssc.ac.cn)

14

15 **Key Points:**

16 □ The seasonal and linear variations of zonal winds coincide with those of MERRA2 with slight differences in
17 magnitudes.

18 □ The responses of zonal winds to QBO are approximately hemispheric symmetry and change from positive to negative
19 with the increasing height.

20 □ The responses of zonal winds to F10.7 and ENSO are more prominent in the southern stratospheric polar jet region as
21 compared to that the northern counterpart.

22



23 Abstract

24 Variations of global wind are important in changing the atmospheric structure and circulation, in the coupling of
25 atmospheric layers, in influencing the wave propagations. Due to the difficulty of directly measuring zonal wind from the
26 stratosphere to the lower thermosphere, we derived the global balance wind (BU) from 2002 to 2019 using the gradient wind
27 approximation and SABER temperatures and modified by meteor radar observations at the equator. These capture the main
28 feature of global monthly mean zonal wind and can be used to study the variations (i.e., annual, semiannual, terannual, and
29 linear) of zonal wind and the responses of zonal wind to QBO (quasi-biennial oscillation), ENSO (El Niño/Southern
30 Oscillation), and solar activity. Same procedure is performed on the MERRA2 zonal wind (MerU) to validate BU and its
31 responses below 70 km. The annual, semiannual, terannual oscillations of BU and MerU have similar amplitudes and phases.
32 The semi-annual oscillation of BU has peaks around 80 km, which are stronger in the southern tropical region and coincide
33 with previous satellite observations. The responses to QBO shift from positive to negative and extend from the equator to
34 higher latitudes with the increasing height. The responses to ENSO and F10.7 are strongest (positive and negatively,
35 respectively) in the southern stratospheric polar jet region below 70 km and exhibit hemispheric asymmetry. While above 70
36 km, the responses of BU to F10.7 and ENSO are mainly positive. Both BU and MerU exhibit similar linear changes, but the
37 negative linear changes of BU at 50°N are absent in MerU during October–January. The discussions on the possible
38 influences of the temporal intervals and sudden stratospheric warmings (SSWs) on the variations and responses of BU
39 illustrate that: (1) the seasonal variations and the responses to QBO are almost independent on the temporal intervals selected;
40 (2) the responses to ENSO and F10.7 are robust but slightly dependent on the temporal intervals; (3) the linear changes of
41 both BU and MerU depend strongly on the temporal intervals; (4) SSWs affect the magnitudes but do not affect the
42 hemispheric asymmetry of the variations and responses of BU at least in the monthly mean sense. The variations and
43 responses of global zonal wind to various factors are based on BU, which is derived from observations, and thus provide a
44 good complementary to model studies and ground-based observations.

45 1 Introduction

46 Atmospheric dynamics field (temperature, wind, etc.) and species not only exhibits latitude, longitude, and height
47 variations, but also exhibits temporal variations with periods ranging from days, months to years, and even decade. The
48 temporal variations can be ascribed into long-term variations, intra-annual and inter-annual variations. Here the long-term
49 variations mean the linear term or linear changes in a regression model and on a time scale longer than one solar cycle in the
50 middle and upper atmosphere. The long-term variations of the middle and upper atmosphere have been received attentions
51 due to the greenhouse gas driven anthropogenic climate change and its influences on atmospheric drag and thus our space
52 vehicles (Beig et al., 2003; Beig et al., 2008; Laštovička, 2017; Yue et al., 2019b; Mlynczak et al., 2022). The intra-annual
53 variations mainly include annual (AO), semi-annual (SAO), and ter-annual (TAO) oscillations. These variations are mainly
54 cause by the revolution of earth with oblique axis relative to the ecliptic plane. Their amplitudes depend on latitude and
55 height (Dunkerton, 1982; Garcia et al., 1997; Randel et al., 2004; Smith et al., 2017).



56 The inter-annual variations are mainly caused by the coupling among different atmospheric layers, sea surface
57 temperature and solar activity. Such as: the QBO (quasi-biennial oscillations) in the tropical regions has periods of 2–3 years
58 due to wave-mean flow interactions. QBO signal can also be seen in the mesosphere, which is anti-phase to the stratospheric
59 QBO due to the selective critical-layer filtering (Baldwin et al., 2001; Burrage et al., 1996; Xu et al., 2007). Recent studies
60 revealed that the mesospheric QBO is a seasonally locked phenomenon and occurs only in vernal equinox when the
61 westward winds enhanced every 2 or 3 years and might be an ephemeral phenomenon (Venkateswara Rao et al., 2012;
62 Kumar, 2021); the ENSO (El Niño/Southern Oscillation) is used to characterized the changes in sea surface pressure and
63 temperature (Domeisen et al., 2019a). It has been reported that the slight change of ENSO can affect global middle and
64 upper atmosphere through the coupling of atmosphere and ocean and wave propagation (Randel et al., 2009; Li et al., 2013;
65 Baldwin and O’Sullivan, 1995; Lin and Qian, 2019); the solar activity can be represented by its radiation flux at 10.7 cm
66 (F10.7), its can influence the atmosphere from upper to below through photon absorption and high energy particle
67 precipitation and ion deposition (Li et al., 2011; Beig et al., 2008; Qian et al., 2019; Venkat Ratnam et al., 2019). Moreover,
68 the temporal variations may be coupled among different time scales. Such as: the coupling between SAO and QBO is mainly
69 due to the selectively filtering and absorbing of equatorial waves and gravity waves by QBO winds (Li et al., 2012; Smith et
70 al., 2017); the coupling between QBO and ENSO is mainly due to the stronger wave activity during the warm phase ENSO,
71 this accelerates downward propagation of QBO (Domeisen et al., 2019a; Taguchi, 2010).

72 The variations and responses of temperature and trace gases (e.g., CO₂, H₂O) in the middle and upper atmosphere have
73 been well studied through observations and model simulations (Laštovička, 2017; Garcia et al., 2019; Lübken et al., 2018;
74 Emmert et al., 2012; Yue et al., 2015, 2019a; Yuan et al., 2019; She et al., 2019; Mlynczak et al., 2022). In contrast, the
75 variations and responses of wind field are more complex than those of temperature due to the direct external forcings and the
76 indirect dynamical coupling of the atmospheric waves and mean flow (Qian et al., 2019). In fact, atmospheric wind field is
77 an important atmospheric parameter since it is a direct driver of atmospheric circulation and influences the atmospheric
78 structure. Moreover, wind field plays important roles in transporting mass and chemical species, in distributing and re-
79 distributing momentum and energy, and in modulating the propagation and dissipation of atmospheric waves (i.e., gravity
80 waves, tides, and planetary waves). This in turn affects the atmospheric circulation and structure indirectly. Thus, the
81 variations and long-term variations of winds should also be studied.

82 Ground-based radar observations have revealed long-term variations of mean wind in the mesosphere and lower
83 thermosphere (MLT) region at several stations. The medium frequency (MF) radar observations at Tirunelveli (8.7°N,
84 77.8°E) from 1993 to 2006 showed that the monthly mean zonal wind was dominated by SAO with eastward peak during
85 solstice and exhibited QBO signal with periods 2–3 years (Sridharan et al., 2007). Using the observations by four MF radars
86 and three meteor radars in the latitudes from 21°S to 22°N during 1990–2010, Venkateswara Rao et al. (2012) showed that
87 the zonal wind exhibited both negative and positive trends, which magnitudes depended on stations and the temporal
88 intervals of the observations. By combining the zonal wind at $\sim z=70$ –80 km observed by the rocketsonde, satellite and MST



89 radar over the Indian region (8.5°N to 18.5°N and 69°E to 89°E), Venkat Ratnam et al. (2013) constructed a long-term
90 dataset from 1977 to 2010. They showed a decreasing trend of 2 ms⁻¹/Year (or 20 ms⁻¹/Decade) in February and March at
91 72.5 and 77.5 km (Fig. 2 of their paper). However, the trends are not significant from May to August. These observations
92 coincided with the results simulated by the Thermosphere-Ionosphere-Mesosphere-Electrodynamics General Circulation
93 Model (TIME-GCM) after doubled the CO₂ concentration (Venkateswara Rao et al. 2013). Recently, after extending the
94 observation data to 2016, Venkat Ratnam et al. (2019) found a decreasing trend at $\sim z=60\text{--}80$ km and an increasing trend of
95 4–5 ms⁻¹/Decade at $\sim z=80\text{--}90$ km and below ~ 60 km. Using the temperature and wind simulated by Whole Atmospheric
96 Community Climate Model with eXtended thermosphere and ionosphere (WACCM-X) and the radar observations at Collm
97 (51°N, 13°E) during 1980–2014, Qian et al. (2019) showed that the wind trends and the solar effects were, respectively,
98 order of $\sim \pm 5$ ms⁻¹/Decade and $\sim \pm 5$ ms⁻¹/100SFU (1 SFU=10⁻²² Wm⁻²Hz⁻¹) but with large standard deviations. Using the
99 historical simulations by WACCM6 during 1850–2014 (165 years), Ramesh et al. (2020) showed the responses of the
100 temperature and zonal wind to QBO, ENSO, solar activity, ozone depleting substance, carbon dioxide, and sulfate aerosol
101 from the stratosphere to the lower thermosphere. They showed that the influences of solar activity are mainly in the
102 mesosphere while the influences of QBO and ENSO are mainly in the stratosphere and mesosphere. Moreover, these
103 influences depend on latitudes.

104 The above observations and modelling studies revealed seasonal variations of zonal winds and their responses to QBO,
105 ENSO, solar activity in the mesosphere. However, the reported long-term (or linear) changes of zonal winds depended on
106 specific locations and the temporal intervals of the data. At present, it is still a challenge to directly measure the atmospheric
107 wind field from the stratosphere to the lower thermosphere. It is compelling to develop a wind dataset to represent the main
108 features of global zonal winds and their temporal variations. Recently, we developed a dataset of global monthly zonal mean
109 zonal wind (short for BU) based on the gradient balance wind theory (Fleming et al., 1990; Randel, 1987; Smith et al., 2017;
110 Xu et al., 2009) and the temperature and pressure profiles measured by the Sounding of the Atmosphere using Broadband
111 Emission Radiometry (SABER) instrument (Russell III et al., 1999). To overcome the tidal alias above 80 over the Equator
112 (Smith et al., 2017; Xu et al., 2009a), we replaced the BU with the zonal wind observed by a meteor radar at Koto Tabang
113 (0.2°S, 100.3°E) (Matsumoto et al., 2016; Hayashi et al., 2013). The BU covers a latitude range of 50°S–50°N and height
114 range 18–100 km and a temporal range of 2002–2019. The BU coincided generally with re-analysis data, empirical wind
115 models and observations by meteor radars and lidar (Liu et al., 2021). Thus, the BU is a reasonable candidate to monthly
116 mean zonal wind and can be used to study the variations and responses of global zonal winds to various factors.

117 The solar activity effects on winds in the MLT region are still unclear (Qian et al., 2019; Venkateswara Rao et al.,
118 2012). It should be noted that the linear changes and solar activity have influences on other signals (i.e., QBO, ENSO), one
119 must isolate the contributions of different signals to get a clearer picture of the variations and responses of zonal winds. The
120 long temporal (18-year) and entire height (18–100 km) intervals of BU are suitable to study the variations of zonal winds and
121 their responses to QBO, ENSO, and solar activity. To separate the relative contributions of the variations and effects of QBO,



122 ENSO, and solar activity to zonal winds, the multiple linear regression (MLR) method will be used.

123 To evaluate the reliability of BU and the corresponding responses below 70 km in further, we will perform the same
124 MLR on the zonal wind of Modern-Era Retrospective analysis for Research and Applications, version 2 (MERRA2). BU
125 will provide the unique wind results at 70–100 km. MERRA2 provides assimilated meteorological field from surface to ~75
126 km (72 levels). It has temporal, longitude, and latitude interval of 3 hours, 0.625°, and 0.5°, respectively (Molod et al., 2015;
127 Gelaro et al., 2017). Each MERRA2 zonal wind profile is interpolated to uniform vertical grid with a step of 1 km. Then the
128 monthly zonal mean wind (MerU) is calculated by averaging these profiles in a latitude band of 5° with an overlap of 2.5° in
129 each month. The variations of MerU and their responses to QBO, ENSO, and solar activity are studied to compare with those
130 of BU below 70 km. MERRA2 is used here due to its good consistency with other data set. Such at the consistency of the
131 monthly mean zonal winds between MERRA2 and the QBO wind at Singapore (Coy et al., 2016), the consistency of the
132 changes in subtropical and polar jets between MERRA2 and other re-analyses (e.g., MERRA, ERA-Interim, JRA-55, and
133 NCEP CFSR) (Manney and Hegglin, 2018).

134 2 Data and multiple linear regression

135 2.1 BU data and reference time series

136 The detailed description and validation of BU can be found in Liu et al. (2021). Here, we provide a short summary of
137 this dataset. The BU dataset includes the monthly mean zonal wind in the height range of 18–100 km and at latitudes of
138 50°S–50°N from 2002 to 2019. BU is mainly derived from the temperature and pressure observations by the SABER
139 instrument (Russell III et al., 1999) and based on the gradient wind theory (Fleming et al., 1990; Randel, 1987; Smith et al.,
140 2017; Xu et al., 2009),

$$141 \frac{\bar{u}^2}{a} \tan \varphi + f \bar{u} = -\frac{1}{a \bar{\rho}} \frac{\partial \bar{p}}{\partial \varphi} \quad (1)$$

142 Here, $f = 2\Omega \sin \varphi$ is the Coriolis factor, $\Omega = 2\pi/(24 \times 60 \times 60)$ is the earth rotation frequency (unit of $\text{rad}\cdot\text{s}^{-1}$), a is the
143 radius of the earth. \bar{u} and $\bar{\rho} = \bar{p}/R\bar{T}$ are the BU and zonal mean density, respectively. R is the gas constant for dry air. At
144 the equator and above 80 km, the tidal alias on gradient wind is replaced by the monthly mean zonal wind measured by a
145 meteor radar at 0.2°S (Matsumoto et al., 2016; Hayashi et al., 2013). The comparisons between BU and other data
146 (MERRA2, HWM14 empirical model, meteor radar and lidar observations at seven stations from around 50°N to 29.7°S)
147 illustrate good agreement. The good agreement suggests that BU is a reasonable candidate to monthly mean zonal wind. The
148 large vertical extent and the 18-year internally consistent time series of BU makes it is suitable to study the variations and
149 responses to solar activity, and QBO, ENSO.

150 The reference time series of solar activity, QBO, and ENSO are used to explore their possible influences on global zonal
151 wind. The solar activity is represented by the solar radio flux at 10.7 cm in a 100-MHz band (F10.7, Fig. 1a, Tapping, 2013).
152 The QBO is represented by the zonal wind at 30 hPa (~25 km) and 10 hPa (30 km) (referred as QBO₃₀ and QBO₁₀ in Fig. 1c)
153 over Singapore (1°N, 104°E) (Baldwin et al., 2001). Due to the propagation nature of QBO with height, we use the QBO



154 winds at two different heights to represent the phase information of QBO. ENSO is represented by the Multivariate ENSO
 155 index (MEI, Fig. 1e, Zhang et al., 2019; Wolter and Timlin, 2011). These reference time series play important roles in
 156 studying the atmospheric coupling and have been widely used to study their influences on temperature, gravity waves, ozone,
 157 and carbon dioxide in the stratosphere and mesosphere (e.g., Li et al., 2011; Randel et al., 2017; Liu et al., 2017; Randel and
 158 Cobb, 1994; Yue et al., 2015).

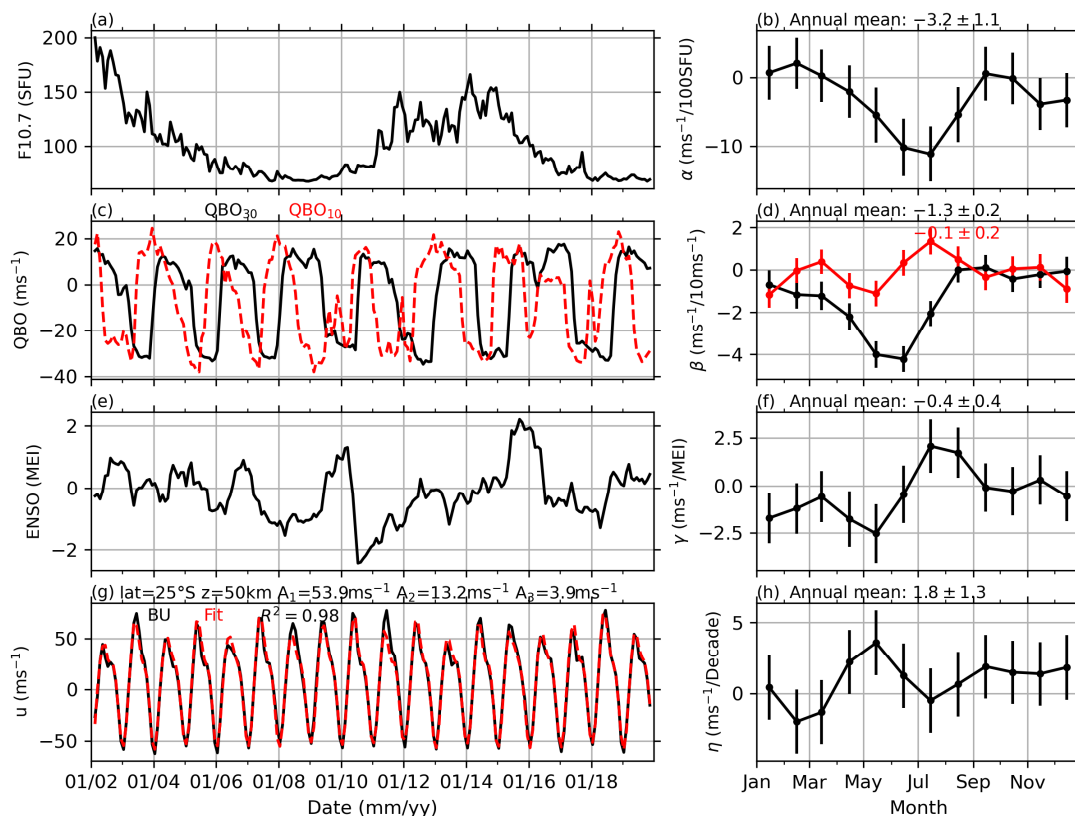


Figure 1: Reference time series and the results of MLR. Left column: (a) solar activity (F10.7), (c) QBO at 30 hPa (black) and 10 hPa (red), (e) ENSO, (g) BU (black solid) and its fitting result (red-dashed line). The amplitudes of AO (A_1), SAO (A_2), and TAO (A_3) and R^2 are labelled on the top of Fig. 1g. Right column: the monthly responses and their standard deviations (σ) of BU to solar activity (b), QBO (d, black and red represent the responses to QBO wind at 30 and 10 hPa, respectively), ENSO (f), and the linear variations of BU (h) in each month. The annual means of the responses and their standard deviations are labeled on the top of each panel.



159 2.2 Multiple linear regression

160 Multiple linear regression (MLR) model is used to isolate the seasonal variations of BU and the possible influences of
161 F10.7, QBO₃₀, QBO₁₀ and MEI on BU (Liu et al., 2017; Li et al., 2011; Randel and Cobb, 1994; Venkat Ratnam et al., 2019).
162 At each latitude and height, the regression model is written as:

$$163 u(t_i) = A_0 + \text{Season}(t_i) + \alpha F10.7(t_i) + \beta_{30} QBO_{30}(t_i) + \beta_{10} QBO_{10}(t_i) + \gamma ENSO(t_i) + \eta t_i + \text{Res}(t_i) \quad (2)$$

$$164 \text{Season}(t_i) = \sum_{k=1}^3 A_k \cos[k\omega(t_i - \varphi_k)]. \quad (3)$$

165 Here, t_i ($i = 1, 2, \dots, N$) is the month number since February 2002. A_0 is the mean wind over the entire temporal interval.
166 $\omega = 2\pi/12$ (month), A_k and φ_k are the amplitude and phase of the annual (AO, $k = 1$), semiannual (SAO, $k = 2$), and
167 terannual (TAO, $k = 3$) oscillations, respectively. The regression coefficients $\alpha, \beta_{30}, \beta_{10}, \gamma, \eta$ include the seasonal variations
168 and have the same form as follows:

$$169 \alpha = \alpha_0 + \sum_{k=1}^3 [\alpha_{2k-1} \cos(k\omega t) + \alpha_{2k} \sin(k\omega t)]. \quad (4)$$

170 Thus, there are 42 parameters to be fitted by the least-squares method. η is the linear variations or long-term trend (Randel
171 and Cobb, 1994). $\text{Res}(t)$ is the residual of the fitting and can be used to estimate the standard deviation of each coefficient
172 with the help of variance-covariance matrix (Kutner et al., 2004). The rationality of the fitting result is quantified by R^2
173 score, which is the variations of the raw data explained by the model and defined as follows:

$$174 R^2 = 1 - \frac{\sum_{i=1}^N \text{Res}^2(t_i)}{\sum_{i=1}^N [u(t_i) - \bar{u}]^2}, \quad \bar{u} = \frac{1}{N} \sum_{i=1}^N u(t_i). \quad (5)$$

175 The best fitting results in $R^2 = 1$, which means that the fitting result is the same as the raw data. For illustrative purpose,
176 BU at 25°S and 50 km (black in Fig. 1g) is taken as an example to show the procedure of MLR. Figure 1(g) shows that the
177 fitting result (red) coincides well with BU with $R^2 = 0.98$. This means that Eq. (2) explains 98% of the variations of BU.
178 Thus, good consistency and large R^2 indicate that BU can be explained well by Eq. (2). The rationality of the fitting results
179 (R^2) at other latitudes and heights will be shown in Sect. 3.1. Figure 1(g) also shows that the AO has amplitude of $A_1 = 53.9$
180 ms^{-1} and is in the dominant position. Then the SAO has a smaller amplitude of 13.2ms^{-1} . While the TAO is weakest and has
181 amplitude of 3.9ms^{-1} .

182 The right column of Fig. 1 shows the monthly responses of BU to solar activity (b), QBO (d), ENSO (f) and the linear
183 variations of BU (h), as well as their standard deviations (σ). Their annual means are labelled on the top of each panel. The
184 response of BU to solar activity (Fig. 1b) has an annual mean of $-3.2 \pm 1.1 \text{ms}^{-1}/100 \text{SFU}$. This negative response is mainly
185 contributed from May–August, in which the negative peaks reach a value of $-10 \text{ms}^{-1}/100 \text{SFU}$ in June and July. In January–
186 April and September–October, the responses of BU to solar activity are less than the standard deviations (σ). This indicates
187 that the responses of BU to solar activity are stronger in winter months and weaker in other months at least for the case
188 shown here. The responses of BU to QBO₃₀ and QBO₁₀ (Fig. 1d) have annual means of $-1.3 \pm 0.2 \text{ms}^{-1}/10 \text{ms}^{-1}$ and -0.1 ± 0.2
189 $\text{ms}^{-1}/10 \text{ms}^{-1}$. The monthly response of BU to QBO₃₀ has negative peaks of $-4 \text{ms}^{-1}/10 \text{ms}^{-1}$ in April–July, when QBO₃₀
190 reaches its eastward or westward peaks. The response of BU to ENSO (Fig. 1f) has an annual mean of $-0.4 \pm 0.4 \text{ms}^{-1}/\text{MEI}$.



191 The monthly responses of BU to ENSO have negative peak in April and positive peaks in July and August. The annual mean
192 linear variations (Fig. 1h) is of $1.8 \pm 1.3 \text{ ms}^{-1}/\text{Decade}$. The monthly linear variation reaches a peak of $3 \text{ ms}^{-1}/\text{Decade}$ in May.
193 We note that the linear variation depends highly on the temporal span of the data and will be discussed in Sect. 4.1.

194 3 Seasonal variations and regression results

195 3.1 Seasonal variations

196 Figure 2 shows the amplitudes and phases of the seasonal variations of BU (upper row) and MerU (lower row). The R^2
197 scores (the fourth column) of both BU and MerU are larger than 0.8 in most region and indicate that the variations of BU and
198 MerU can be explained well by Eq. (2). However, at 50°N/S around 90 km and in the tropical regions above 95 km, the R^2
199 scores of BU are less than 0.6. This indicates that the variabilities of BU are influenced by some other factors, which were
200 not included in Eq. (2). These factors might include (1) the phase change (eastward peak shifting from winter to summer) of
201 zonal wind caused by the strong gravity waves dissipation at high latitudes (Liu et al., 2022), (2) the strong tides and short-
202 term variabilities of zonal wind in the equatorial lower thermosphere (Xu et al., 2009b; Smith et al., 2017; Liu et al., 2021),
203 and (3) the imperfect BU in the extra-tropical lower thermosphere (Liu et al., 2021).

204 The latitude-height distributions of the amplitudes and phases of AO of BU and MerU exhibit general consistencies and
205 slight discrepancy. The consistencies include that: (1) both BU and MerU have peaks around 55 km in July in the Southern
206 Hemisphere (SH) and around 65 km in January in the Northern Hemisphere (NH); (2) both BU and MerU have small
207 amplitude below ~ 30 km at all latitudes and throughout the height range in the tropical regions. The discrepancy is that the
208 AO of MerU has larger amplitudes in the SH but smaller amplitudes in the NH than that of BU. The possible reason for the
209 weaker AO in MerU in the NH has peak around 65 km, which might be caused by the damping layers of MERRA2 and
210 reduced the zonal wind (Ern et al., 2021). Above 80 km, the amplitude of AO is small. This is because the magnitudes of
211 zonal wind above 80 km are slower than those at around 60 km, where the stratospheric polar jet occurs.

212 The SAO of both BU and MerU have nearly identical phases in the regions where their amplitudes are prominent. The
213 amplitudes of the SAO of both BU and MerU exhibit hemispheric asymmetry. At latitudes higher than 35°S , the SAOs of
214 both BU and MerU have peaks at $\sim z=35\text{--}55$ km. However, above 65 km, the SAO of BU is stronger than that of MerU. In
215 the tropical regions, the SAOs of both BU and MerU are stronger in the SH than that in the NH. This coincides with the
216 measurements by High Resolution Doppler Imager (HRDI) measurements, the assimilated data by U.K. Meteorological
217 Office (UKMO) (Ray et al., 1998), and the balance wind derived from SABER and Microwave Limb Sounder (MLS)
218 observations (Smith et al., 2017). Large discrepancies occur at latitudes higher than 40°N , where the SAO of MerU is much
219 stronger than that of BU below ~ 70 km. Above 70 km, the SAO of BU reproduces the same pattern as that at around 40 km
220 but has larger magnitudes and anti-phase.

221 The TAOs of both BU and MerU have same phases and peaks at $\sim z=30\text{--}60$ km and at latitudes higher than 25°S . In the
222 tropical regions and around 45 km, the TAO of BU has two peaks, which are approximately symmetric to the equator, but



223 the TAO of MerU has one peak over the equator. At $\sim z=50-70$ km, the TAO of BU has larger amplitude than that of MerU.
 224 Above 80 km, the TAO of BU is asymmetric to the equator and has larger peak in the SH tropical region.

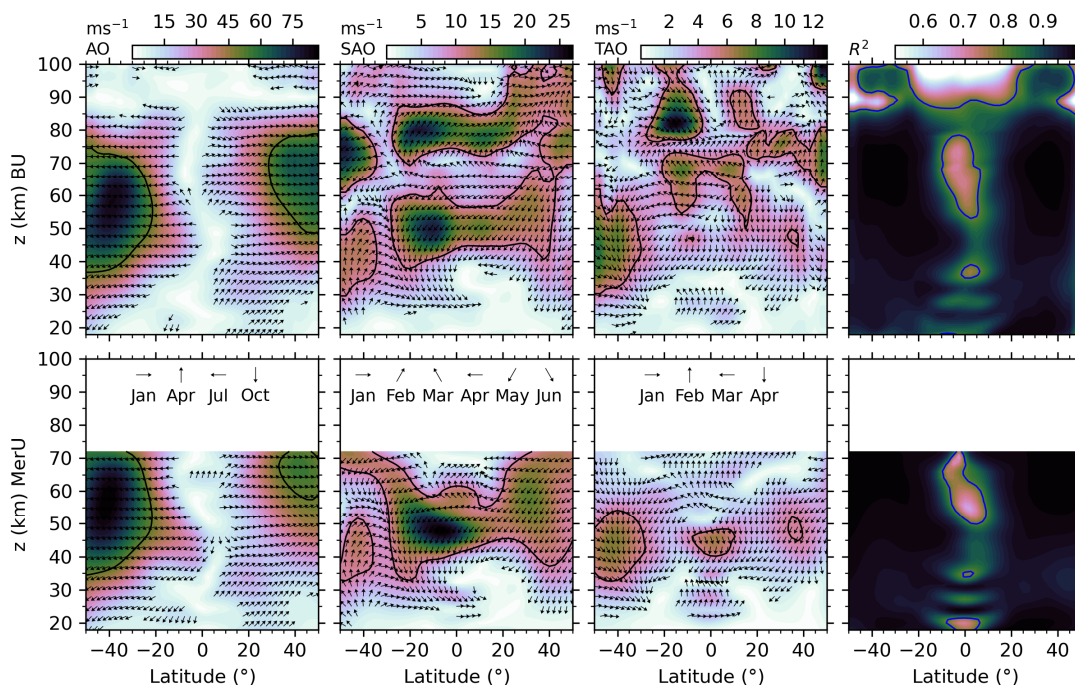


Figure 2: The latitude-height distributions of the amplitudes (color) and phases (indicated by arrow directions) of the AO, SAO, TAO, and the R^2 scores (from left to right). The contour lines of the AO, SAO, TAO, and the R^2 scores indicate 50 ms^{-1} , 10 ms^{-1} , 5 ms^{-1} , and 0.8 , respectively.

225 A short summary is that AO, SAO, and TAO of both BU and MerU have nearly identical phases in the regions where
 226 their amplitudes are prominent. Their consistencies are better in the SH than in the NH on the aspects of both patterns and
 227 magnitudes. The discrepancies of these seasonal variations are mainly in the NH. Above 70 km, the weak AO due to the
 228 weaker wind as compared to that in the stratospheric jet region. The SAOs around 50 km and 80 km are hemispheric
 229 asymmetric and stronger in the SH, which coincides with the HRDI observations (Ray et al., 1998) and the balance wind
 230 (Smith et al., 2017). The TAO of BU above 80 km is hemispheric asymmetric and stronger in the SH.

231 3.2 Responses to solar activity

232 The latitude-height distributions of the responses of BU and MerU to F10.7 (upper two rows of Fig. 3) exhibit general



233 consistencies in January and July and in the annual mean. These consistencies include: (1) the positive response at $\sim z=40\text{--}60$
234 km and around 40°N in January; (2) the negative response above 60 km at $\sim 20^\circ\text{S}$ in January; (3) the negative response in
235 July extending from the SH stratospheric jet region to $\sim 30^\circ\text{N}$. In contrast, the discrepancies are: (1) stronger negative
236 response of BU in January at 50°N , as compared to that of MerU; (2) the negative responses of BU in October around 65 km
237 and above the equator, which cannot be seen in MerU. The annual mean responses of BU and MerU are: (1) mainly negative
238 in the regions extending from $\sim 30^\circ\text{S/N}$ to higher latitudes with the increasing height; (2) mainly positive (negative) in the
239 tropical regions below ~ 30 km (around ~ 40 km). Above ~ 80 km, an interesting feature is that the positive responses of BU to
240 F10.7 are approximately hemispheric symmetry, i.e., at $25^\circ\text{S}\text{--}5^\circ\text{S}$ in January and at $5^\circ\text{N}\text{--}25^\circ\text{N}$ in July. The annual mean
241 responses of BU to F10.7 are mainly positive at $60\text{--}80$ km. Above ~ 90 km, the annual mean responses of BU to F10.7 are
242 mainly positive around the equator and negative at higher latitudes. This feature has a similar pattern but larger amplitude as
243 compared to the results simulated by WACCM-X (Ramesh et al., 2020).

244 The monthly-height distributions of the responses of BU and MerU to F10.7 (lower two rows of Fig. 3) exhibit general
245 consistencies below ~ 70 km. However, the discrepancies should be clarified. Such as: the stronger negative responses of BU
246 in winter months (June–September at 50°S and December–January at 50°N); the weaker positive responses of BU at the
247 equatorial lower height as compared to that of MerU. It should be noted that the negative responses of winds at the southern
248 and northern high latitudes can also be seen in the results simulated by WACCM-X (Ramesh et al., 2020).

249 The MF radar observations at Langfang (39.4°N , 116.7°E) revealed a positive correlation between zonal wind and solar
250 activity from 2009 to 2020 during spring and summer at $80\text{--}84$ km (Cai et al., 2021). However, another MF radar
251 observations at Juliusruh (54.6°N , 13.4°E) revealed that the correlations between zonal wind and solar activity from 1990
252 and 2005 were positive during winter but negative in summer (Keuer et al., 2007). Our results coincide with the observations
253 at Langfang but different from those at Juliusruh. The simulation study by Qian et al. (2019) showed that the solar activity
254 effects on global zonal wind are sporadic in latitude and height distributions. They suggested that the zonal wind might be
255 influenced by both the direct effects of solar radiance and the indirect effects of dynamic process such as wave-mean flow
256 interaction. Qian et al. (2019) also proposed that the temporal intervals of data should be specified when we study the trends
257 and solar activity effects since the trend drivers are different in different periods. This will be discussed in Sect. 4.1.

258 A short summary is that the annual mean responses of both BU and MerU to F10.7 are more negative in the
259 stratospheric polar jet region of SH than that of NH. Above the stratospheric polar jet, the responses of BU change from
260 negative to positive with the increasing height at latitudes higher than 15°N/S . Around ~ 80 km, the annual responses of BU
261 to F10.7 are mainly positive in the tropical region.

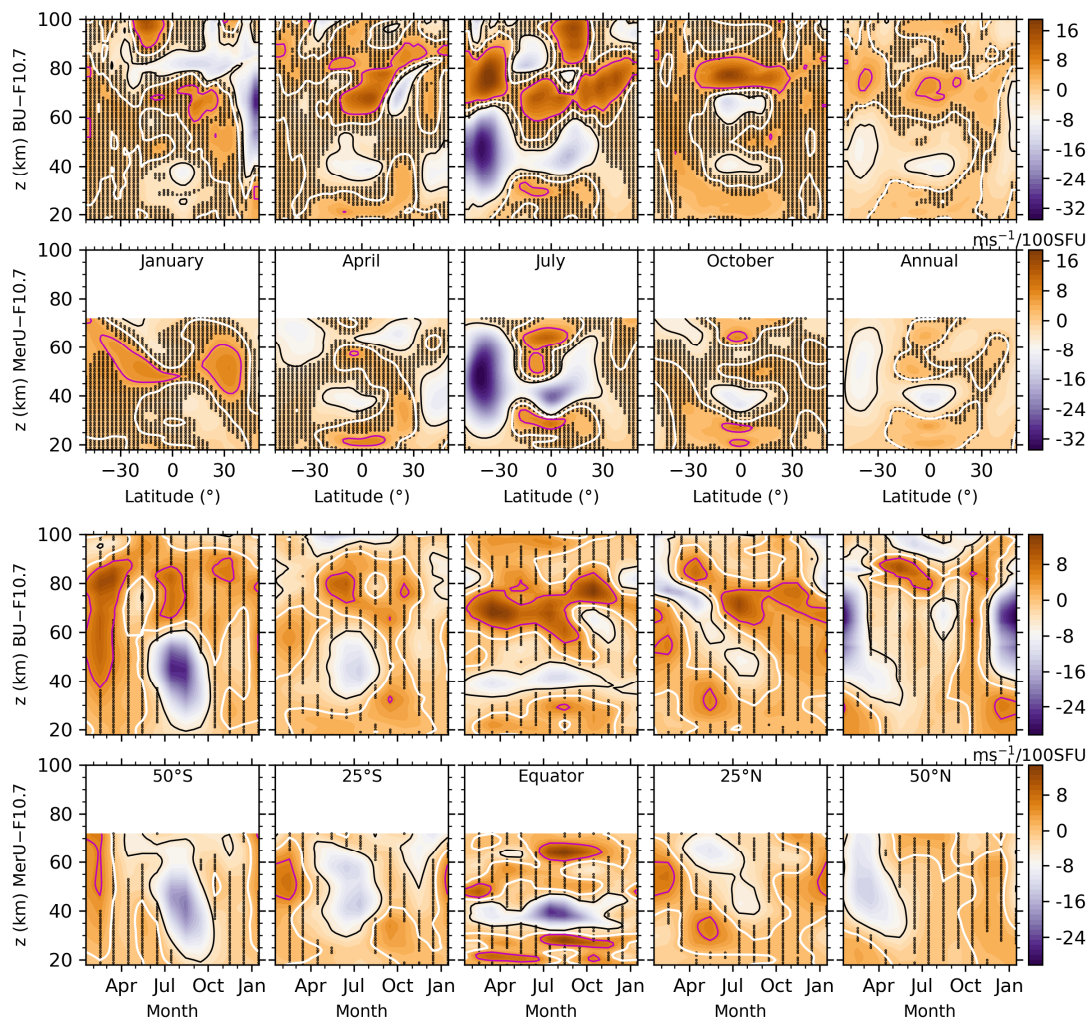


Figure 3: Upper two rows: latitude-height distributions of the regression coefficients of BU (the first row) and MerU (the second row) to F10.7 in January, April, July, October, and annual mean (from left to right). Lower two rows: monthly-height (lower two rows) distributions of the regression coefficients of BU (the third row) and MerU (the fourth row) to F10.7 at 50°S–50°N with interval of 25° (from left to right). The black dots indicate that the regression coefficients are less than one σ . The magenta, white, and black contour lines indicate the regression coefficients of 5, 0, and -5 $\text{ms}^{-1}/100 \text{ SFU}$,



respectively.

262 3.3 Responses to QBO

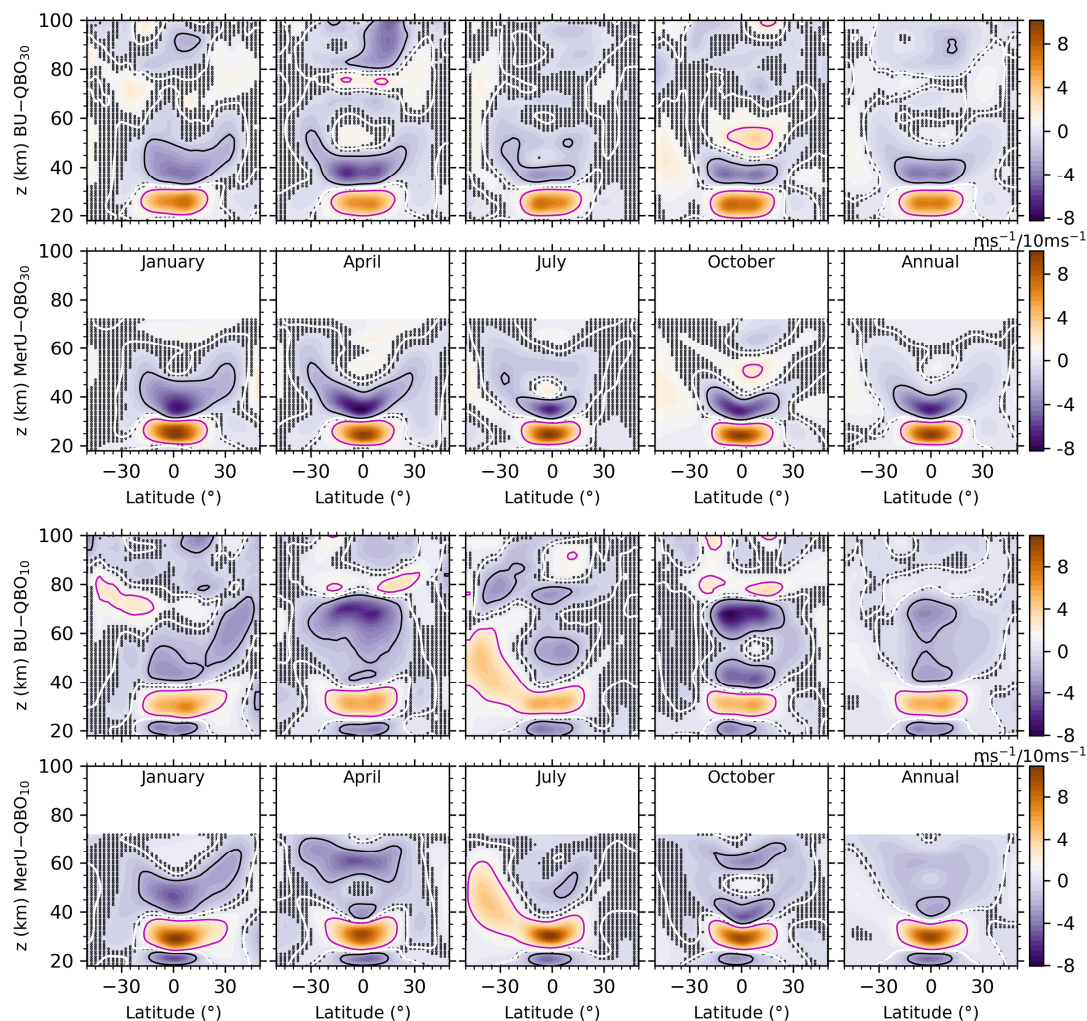


Figure 4: Same captions as the upper two rows of Fig. 3 but for the responses to QBO₃₀ and QBO₁₀, respectively. The magenta, white, and black contour lines indicate the regression coefficient of 2, 0, and $-2 \text{ ms}^{-1}/10 \text{ ms}^{-1}$, respectively.



263 The latitude-height distributions of the responses of BU and MerU to QBO₃₀ (upper two rows of Fig. 4) exhibit general
264 consistencies in all months and in the annual mean below ~50 km. Such as the responses of BU and MerU to QBO₃₀ change
265 from positive below 30 km to negative at $z=30-50$ km and $25^{\circ}\text{S}-25^{\circ}\text{N}$. The varying responses with height are mainly due
266 to the downward propagation of QBO phase with time. This can be confirmed by the responses of BU and MerU to QBO₁₀ at
267 a higher height (lower two rows of Fig. 4), where the responses of BU and MerU to QBO₁₀ change from negative to positive
268 and then negative again. The discrepancy is that the responses of BU to QBO₃₀ and QBO₁₀ are slightly weaker than those of
269 MerU below ~50 km.

270 The responses of BU to QBO₃₀ are weaker at ~50–80 km. As the height increases, the responses of BU to QBO₃₀
271 become stronger again and have peak around ~90 km. This coincides with the mesospheric QBO, which is antiphase with the
272 stratospheric QBO and extends to $30^{\circ}\text{S}-30^{\circ}\text{N}$ as revealed by High Resolution Doppler Imager observations (HRDI)
273 (Burrage et al., 1996), TIMED Doppler Interferometer observations (Kumar, 2021) and reviewed by Baldwin et al., (2001).
274 This coincides also with the results simulated by WACCM6 on the aspects of the hemispheric asymmetry, i.e., the responses
275 extending to higher southern (northern) latitudes in summer (winter) (Ramesh et al., 2020). Moreover, the annual mean
276 responses of BU and MerU to QBO₃₀ and QBO₁₀ are positive and are more significant at 50°S than those at 50°N at $z=50-$
277 80 km. The significant positive responses at 50°S are mainly contributed by those in July and October around 50 km, where
278 and when the stratospheric polar jet occurred.

279 A short summary is that the influences of the stratospheric QBO extend from the equator to higher latitudes. The
280 influences can be positive or negative, which depend on heights and latitudes. Such as the negative influences above ~80 km
281 in the tropical region and the positive influences at the southern high latitudes. Above ~80 km, the negative responses of
282 winds to the stratospheric QBO are hemispheric asymmetry and are more negative in the NH tropical regions.

283 3.4 Responses to ENSO

284 The latitude-height distributions of the responses of BU and MerU to MEI (upper two rows of Fig. 5) generally coincide
285 with each other in all months and in the annual mean. In January and at $z=40-60$ km and latitudes higher than 40°N ,
286 although the responses of MerU and BU to MEI are positive, the responses of BU to MEI are not significant. This coincides
287 with the results simulated by WACCM6, which were positive but were lower than the 95% confidence level (Ramesh et al.,
288 2020). In April and October, and at ~35 km, the negative responses of winds to MEI are approximately hemispheric
289 symmetric. The annual mean responses of both winds to MEI are stronger and wider in the SH than those in the NH. In July
290 and at ~50 km, the responses of both winds are positive with peaks around $\sim 40^{\circ}\text{S}$. This indicates that the positive MEI index
291 (warm phase of ENSO or El Niño event) increases the eastward zonal winds. In July and at $z=65-80$ km, the negative
292 responses have peaks around the equator and 35°N/S . Above 60 km, the positive responses of winds to MEI tilt from higher
293 height (~90 km) at 35°S to a lower height (~80 km) at 35°N in January. This pattern continues in April and July. Above ~90
294 km and around $\sim 15^{\circ}\text{S}$, the responses of BU to MEI are positive in January and negative in July. The annual mean responses



295 are mainly positive in most latitudes.

296

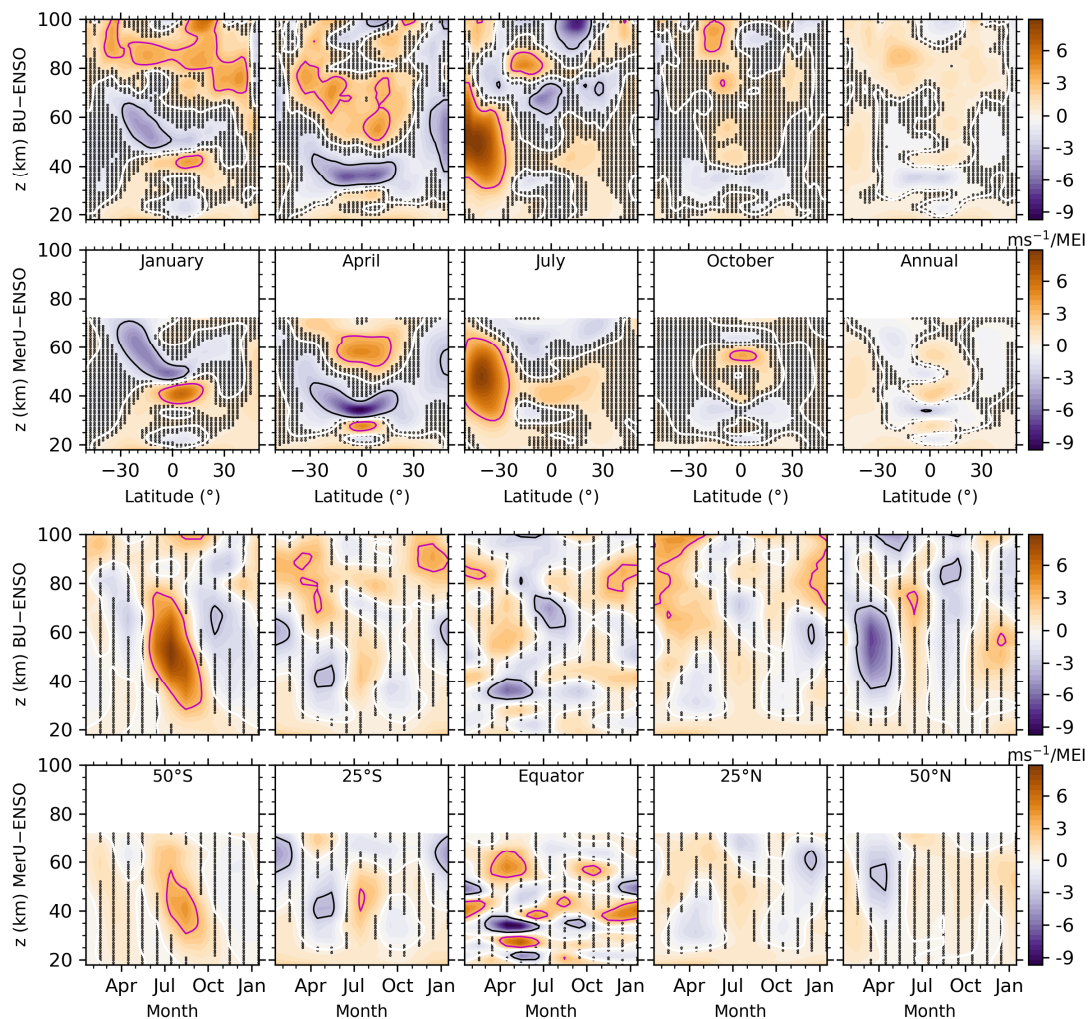


Figure 5: Same caption as Figure 3 but for the responses to ENSO. The magenta, white, and black contour lines indicate the regression coefficient of 3, 0, and -3 $\text{ms}^{-1}/\text{MEI}$, respectively.

297 The monthly-height distributions of the responses of BU and MerU to MEI (lower two rows of Fig. 5) generally



298 coincide with each other at each latitude, except that the responses of BU to MEI have stronger peaks than those of MerU at
299 50°N/S. The prominent responses of winds to MEI are positive at 50°S (tilting from July at higher height to October at lower
300 height) and are negative at 50°N (mainly in March and April). At 25°N/S, the responses of winds to MEI are mainly positive
301 (extending upward to ~50 km and then tilting backward with the increasing height in July and August) and are negative
302 (extending backward and forward below ~60 km). At the equator, the responses of MerU to MEI exhibit larger variabilities
303 than those of BU below ~40 km.

304 Previous studies showed that during El Niño (warm phase of ENSO), the warm sea surface temperature increases the
305 wave activity, which has a high probability of leading to sudden stratospheric warming (SSW) events (Polvani and Waugh,
306 2004). Then the warm temperature and decelerated zonal wind anomalies can be observed in the stratosphere from January
307 to April at 60°N (Manzini et al., 2006; Domeisen et al., 2019b). This can be summarized as a negative response of zonal
308 wind to ENSO at northern high latitudes. This negative response can also be seen at 50°N (lower-right two panels of Fig. 5).
309 Using the WACCM simulations and SABER observations, T. Li et al., (2016) showed that the stratospheric zonal wind is
310 weekend due to the increased stratosphere meridional temperature gradient at the southern high latitudes in December and in
311 the warm phase of ENSO. This supports the weak negative responses of zonal wind to ENSO at 50°S in December (lower-
312 left two panels of Fig. 5). However, Both BU and MerU showed that the responses zonal wind to ENSO are positive from
313 July to October at 50°S. The physics behind this positive response should be further explored through simulation studies.

314 A short summary is that both BU and MerU exhibit similar responses to MEI. Whereas the responses of BU to MEI are
315 stronger than those of MerU at 50°N/S. An interesting feature is that the responses of winds to MEI propagate downward
316 with increasing time at 50°N/S and 25°N/S, especially the positive responses of BU to MEI at 50°S and 25°S.

317 3.5 Linear variations

318 The latitude-height distributions of the linear variations of BU and MerU (upper two rows of Fig. 6) generally coincide
319 with each other in regions where their magnitudes larger than one σ . The consistencies include: (1) in April and around the
320 equator, the positive variations at ~20 km and ~60 km and negative variations at ~35 km; (2) in April and in the annual mean,
321 the negative variations having peaks at 40°N and extending to the northern higher latitudes. The discrepancies of the linear
322 variations between BU and MerU include that: (1) the negative variations of BU around 50°N (50°S) cannot be seen in
323 MerU in January (April); (2) the positive variations of MerU are larger than those of BU above ~55 km. Above 70 km, the
324 patterns of the linear variations of BU are sporadic and strongly dependent on months, latitudes and heights.

325 The monthly-height distributions of the linear variations of BU and MerU (lower two rows of Fig. 6) generally coincide
326 with each other. The negative variations of BU and MerU coincide with each other at 50°S in August–October and at 25°S in
327 May–July. However, the large discrepancy is that the negative variation of BU at 50°N cannot be seen in MerU in October–
328 January. Above ~70 km, the positive variations last a longer time interval as compared to the negative variations.

329

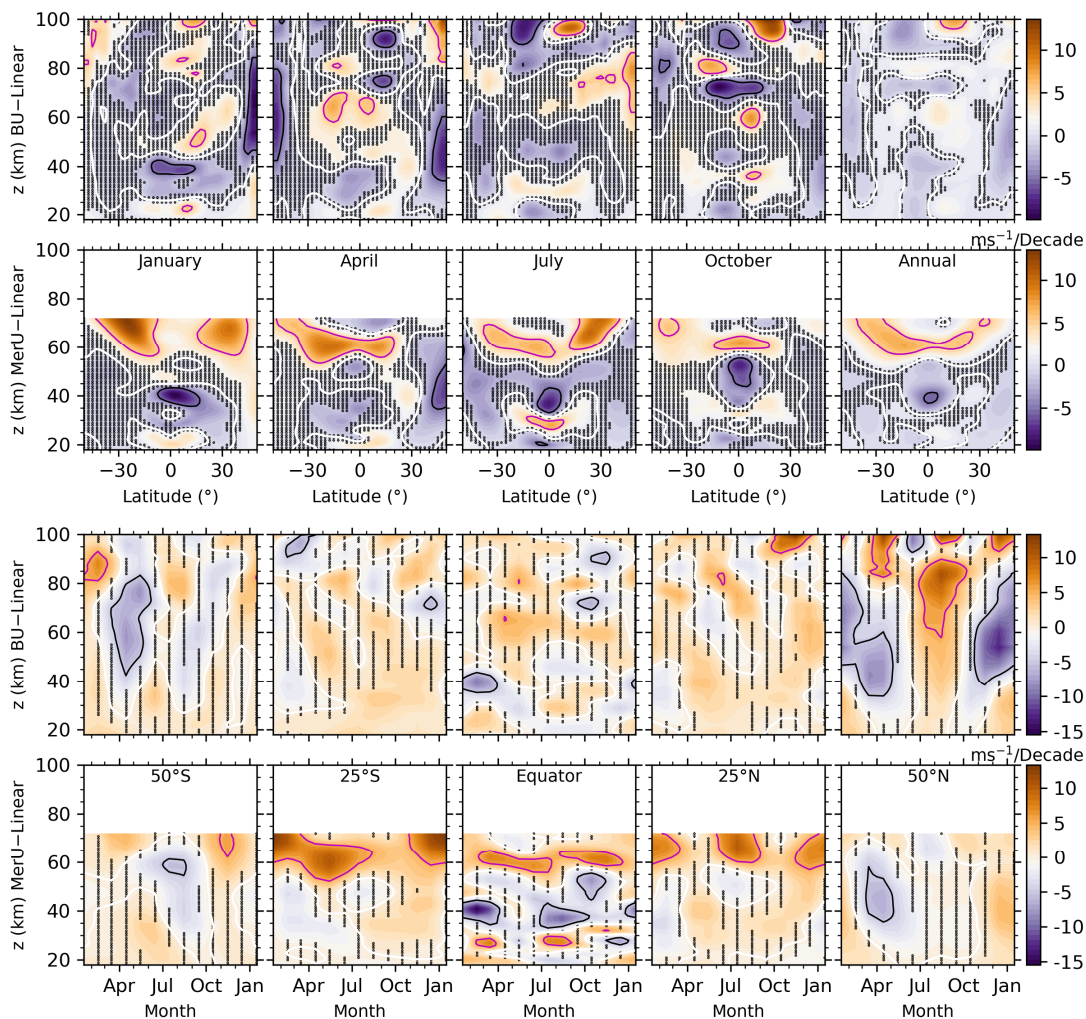


Figure 6: Same caption as Figure 3 but for the linear variations. The magenta, white, and black contour lines indicate the regression coefficient of 5, 0, and $-5 \text{ ms}^{-1}/\text{Decade}$, respectively.

330 Using the MF radar observations at Juliusruh (54.6°N ; 13.4°E) during 1990–2005, Keuer et al. (2007) showed that the
331 zonal wind below 80 km exhibited a negative trend of $\sim -5 \text{ ms}^{-1}/\text{Decade}$ in summer and a positive trend of $\sim 4 \text{ ms}^{-1}/\text{Decade}$ in
332 winter (Fig. 14 of their paper). This result does not coincide with our analysis. By combining the radar, rocketsondes and



333 satellite observations over Indian region and simulation results by WACCM-X, Venkat Ratnam et al. (2019) show a negative
334 trend of $\sim -5 \text{ ms}^{-1}/\text{Decade}$ between 70 and 80 km. This result coincides with our analysis only during April and October. It
335 should be noted that linear variations of zonal wind depend on the station, height range, measuring techniques, and the
336 temporal interval of the data (Keuer et al., 2007; Ramesh et al., 2020). This illustrates the complexity of the linear variations
337 of zonal wind. Moreover, the inhibited linear variations of regressors used in the MLR model and the dynamics (such as
338 SSW) are also important in retrieving the linear variations of zonal winds (Qian et al., 2019). The effects of the temporal
339 coverage of the data and SSWs in the NH on the responses will be discussed in Sect. 4.

340 A short summary is that both BU and MerU exhibit similar linear variations. But this consistency is not as good as that
341 the seasonal variations, the responses to F10.7, QBO, and ENSO. The large discrepancy is that the negative variations of BU
342 at 50°N cannot be seen in MerU in October–January. Above 70 km, the patterns of the linear variations of BU are sporadic
343 and strongly dependent on months, latitudes and heights.

344 4 Discussions

345 4.1 Influences of temporal intervals of data

346 Robust responses or linear variations should not depend on the temporal intervals of the data (Souleymane et al., 2021;
347 Mudelsee, 2019; Qian et al., 2019). This means that the temporal interval of the data should be long enough, which is
348 difficult to be satisfied since the atmospheric variations or oscillations have multiple temporal scales (ranging from month to
349 decade). To test the robustness of the regression results described in Sect. 3, we change the temporal intervals of both BU
350 and MerU according to solar activity, which exhibits nearly 11-year variations. One is 2002–2015, which covers an interval
351 from solar maximum to minimum and then to maximum. The other is 2008–2019, which covers an interval from solar
352 minimum to maximum and then to minimum. After August 2004, the MLS data have been assimilated into MERRA2
353 (Molod et al., 2015; Gelaro et al., 2017). To test the sensitivity to this change, we introduce the third temporal interval of
354 2005–2019. Finally, the fourth temporal interval is 2002–2019, which is the entire data used here.

355 Figure 7 shows the annual mean responses of winds to QBO₃₀ and ENSO in the four temporal intervals. The responses
356 of BU to QBO₃₀ (the first row) are nearly identical among the four temporal intervals throughout the height range. The slight
357 difference is the weaker positive responses of BU to QBO₃₀ during 2005–2019 at $\sim 55 \text{ km}$ around the equator. The responses
358 of MerU to QBO₃₀ (the second row) are also nearly identical among the four temporal intervals throughout the height range.
359 The slight difference is the weaker positive responses (less than one σ) of MerU to QBO₃₀ at $\sim 60 \text{ km}$ around the equator in
360 the temporal span of 2005–2019. These comparisons show that the responses of winds to QBO₃₀ are robust and are almost
361 independent on the temporal intervals.

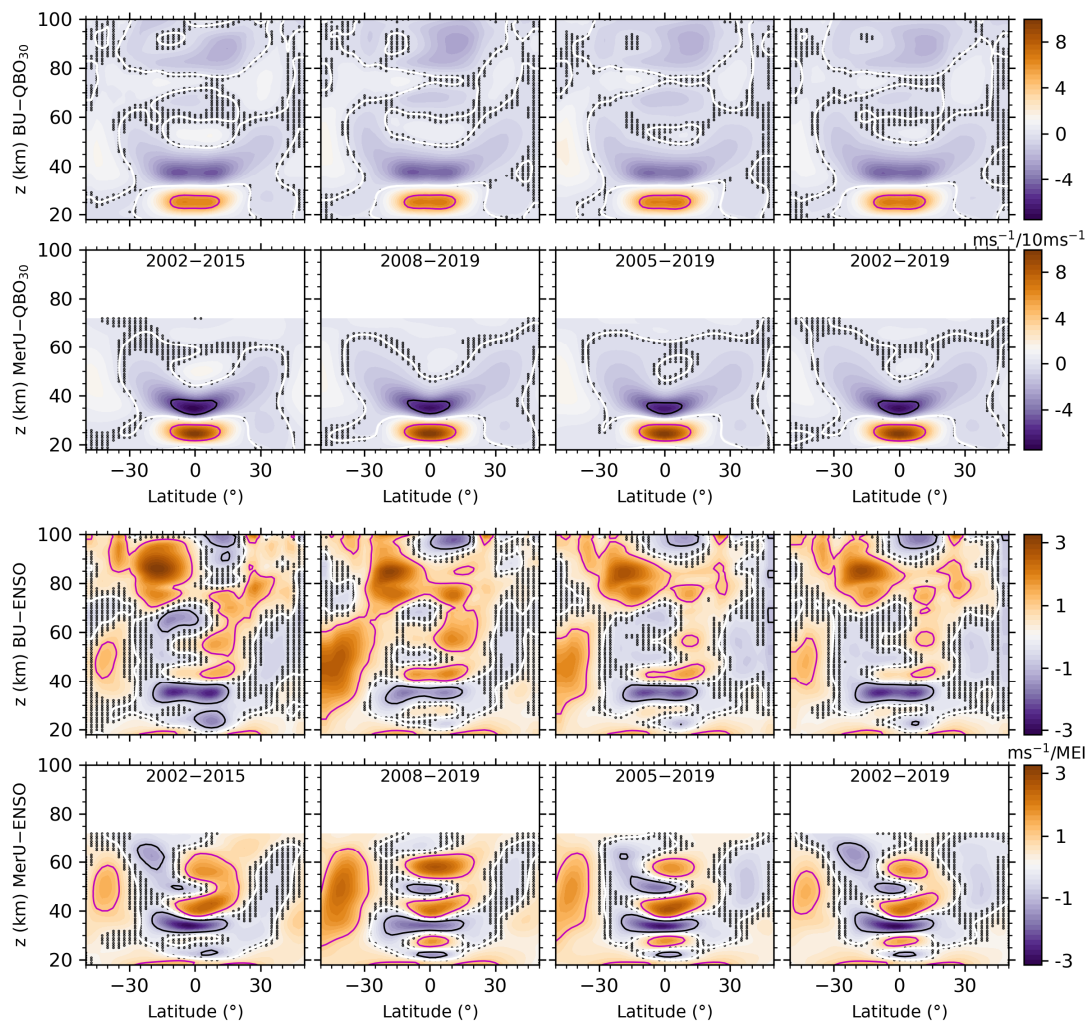


Figure 7: Latitude-height distributions of the annual mean regressions of BU (the first and third rows) and MerU (the second and fourth rows) to QBO30 (upper two row) and ENSO (the lower two rows). The black dots indicate where the regression coefficients less than standard deviations. The magenta, white, and black contour lines in the upper (lower) two rows indicate the regression coefficients of 5, 0, and -5 $\text{ms}^{-1}/10 \text{ms}^{-1}$ (1, 0, and -1 $\text{ms}^{-1}/\text{MEI}$), respectively.

362

The annual mean responses of BU to ENSO (the third row) have similar patterns among the four temporal intervals.



363 Such as: (1) the positive responses extending from the southern high latitudes at lower height to lower latitudes at higher
364 height, (2) the positive responses extend from the tropical regions at ~ 40 km to middle latitudes at higher height, (3) the
365 positive and negative responses shifting with height in the tropical regions below ~ 40 km. The slight difference is the weaker
366 positive at the southern high latitudes and around ~ 50 km during 2002–2015 and 2002–2019, as compared to the other two
367 temporal intervals. The responses of MerU to ENSO (the fourth row) have also similar patterns of responses among the four
368 temporal intervals. This is similar to that of BU and might be caused by the larger variabilities of MEI index after 2008. The
369 negative responses of both winds to ENSO are stronger around $\sim 20^\circ\text{S}$ and ~ 60 km during 2002–2015 and 2002–2019, as
370 compared to other temporal intervals. In a word, the responses of winds to ENSO are robust but slightly depend on the
371 temporal intervals.

372 Figure 8 shows the annual mean responses of winds to F10.7 (upper two rows) and the linear variations of winds (lower
373 two rows) in the four temporal intervals. In the temporal intervals of 2002–2015 and 2002–2019, both BU and MerU exhibit
374 similar responses to F10.7. In the temporal intervals of 2008–2019 and 2005–2019, both BU and MerU also exhibit similar
375 responses to F10.7. In the four temporal spans, the responses of MerU to F10.7 are more negative at latitudes higher than
376 $\sim 30^\circ\text{S}$ and extend to a higher height than those of BU. Around the tropical region and at ~ 40 km, the responses MerU to
377 F10.7 are more negative than those BU. At latitudes higher than $\sim 30^\circ\text{S}$ and around the tropical regions, the positive
378 responses of BU to F10.7 have peaks at $\sim z=70$ – 85 km, which are larger in the temporal intervals of 2002–2015 and 2002–
379 2019, as compared to other temporal intervals. The stronger responses in the temporal intervals of 2002–2015 and 2002–
380 2019 might be caused by the fact that the solar activity has a higher peak in 2002 than in 2014 (Fig. 1a).

381 The linear variations of both BU and MerU depend strongly on the temporal intervals. Among the four temporal
382 intervals, the regions and magnitudes of negative variations are largest and strongest in the temporal span of 2008–2019, and
383 are larger and stronger in the temporal interval of 2005–2019, and then in the temporal interval of 2002–2019. In contrast,
384 the regions and magnitudes of positive variations are largest and strongest in the temporal interval of 2002–2015. Because
385 the dependencies of the linear variations of BU and their dependencies on different temporal interval are similar to those of
386 MerU, we cannot determine whether or not the assimilation of MLS data into MERRA2 influences the linear variations. The
387 possible reasons, which are responsible for the strong dependencies of the linear variations on different temporal intervals,
388 can be ascribed to the different linear variations inhibited in the regressors and the unstable regressors in different temporal
389 intervals (Qian et al., 2019).

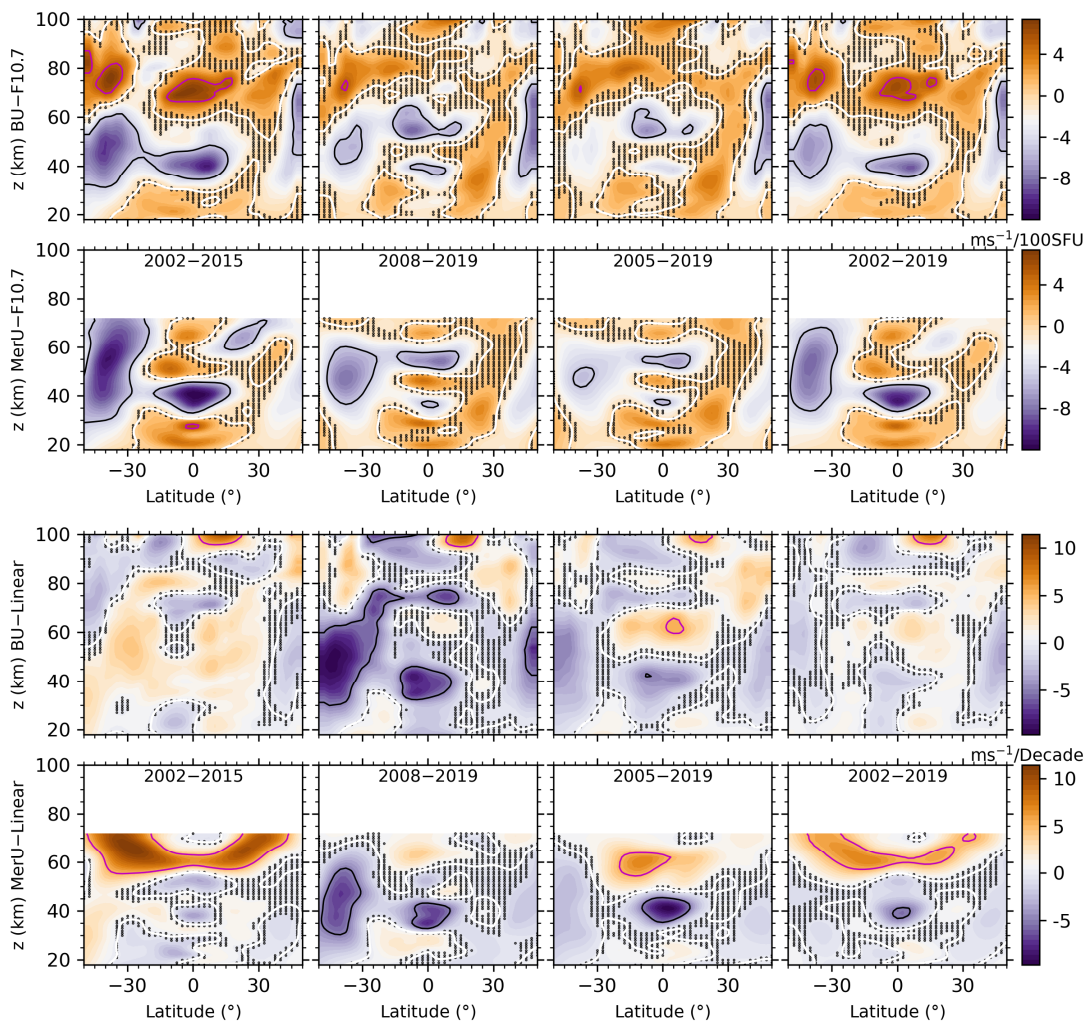


Figure 8: Same caption as Figure 7 but for the responses to F10.7 (upper two rows) and linear trend (lower two rows). The magenta, white, and black contour lines in the upper (lower) two rows indicate the regression coefficients of 5, 0, and $-5 \text{ ms}^{-1}/100 \text{ SFU}$ ($5, 0, \text{ and } -5 \text{ ms}^{-1}/\text{Decade}$), respectively.

390 First, we examine the linear variations inhibited in the regressors (F10.7, QBO, and ENSO) and list their linear slopes in
 391 Table 1. The values in Table 1 are approximate values and are derived through the following steps. From the upper two rows



392 of Fig. 8, we see that the maximum responses of winds to F10.7 is $10 \text{ ms}^{-1}/100\text{SFU}$ ($0.1 \text{ ms}^{-1}/\text{SFU}$). According to this
393 conversion rule, one unit of the linear variation of F10.7 (SFU/Decade) can induce the wind variation of $0.1 \text{ ms}^{-1}/\text{Decade}$.
394 Approximately, one unit of the linear variation of ENSO (MEI/Decade) can induce the wind variation of $1 \text{ ms}^{-1}/\text{Decade}$.
395 Thus, in quality, the combination influences of these regressors can be summarized and listed in the last row of Table 1. We
396 see that the inhibited linear variations of these regressors provide negative (positive) variations in the temporal spans of
397 2002–2015 and 2002–2019 (2008–2019 and 2005–2019). These inhibited linear variations share the linear variations of
398 winds in Eq. (2). The positive (negative) inhibited linear variations make the linear variations winds more negative (positive).
399 This is confirmed by the fact that the regions and magnitudes of linear variations decrease if we remove the linear variations
400 of each regressors (not shown here). This explains partially the strong dependencies of the linear variations on different
401 temporal spans.

402 **Table 1:** Linear variations of F10.7, QBO30, QBO10, and ENSO in different temporal spans and their combination
403 effects on the linear variations of BU

Regressors (unit)	2002–2015	2008–2019	2005–2019	2002–2019
F10.7 (SFU/Decade)	1.1	-3.2	6.7	-17.3
QBO ₃₀ ($\text{ms}^{-1}/\text{Decade}$)	-2.5	0.7	5.6	1.5
QBO ₁₀ ($\text{ms}^{-1}/\text{Decade}$)	2.2	3.6	3.1	0.1
ENSO (MEI/Decade)	-0.1	1.1	0.5	0.1
Combination ($\text{ms}^{-1}/\text{Decade}$)	-0.29	5.08	9.87	-0.03

404 Second, even if we remove the linear variations of each regressors, the dependencies of the linear variations on different
405 temporal spans cannot be removed completely. This might be induced by the fact that the regressors are not stable time
406 series and have varying magnitudes and periodicities in different temporal intervals. Such as the MEI index, which has larger
407 variations after 2009 than before (Fig. 1c); F10.7, which has larger peaks in 2002 than in 2014 (Fig. 1a). It should be noted
408 that each regressor has its own linear variations and varying magnitudes and periodicities, which are the physical nature of
409 the regressor and should not be removed. Such that one can get a reliable response of the winds to each regressor although
410 the responses depend on the temporal interval of the data.

411 The dependencies of winds to QBO are almost identical in different temporal intervals. The dependencies of winds to
412 ENSO on temporal intervals are slightly stronger than to QBO. The dependencies of winds to F10.7 on temporal intervals
413 are stronger than to QBO. The dependency of the linear variations of winds on temporal intervals are the strongest one.
414 Comparing among these responses and the linear variations, we can conclude that the MLR can capture robust responses if
415 the regressor has relatively stable oscillation period and amplitude (i.e., QBO) and the data length is long enough to cover



416 the main features of the regressor. The robustness decreases as the stability (i.e., the magnitudes and periodicities) of the
417 regressor decreases (such as ENSO and F10.7). For the linear variation, its oscillation period can be regarded as infinite. Thus,
418 the data length should be infinite to get a reliable linear variation. However, this is not possible in reality. Consequently, we
419 propose that the linear variations should be examined in different temporal spans, such that one can get a more
420 comprehensive impression on the linear variations although the exact long-term linear variations are unknown.

421 **4.2 Possible reasons of hemispheric asymmetry**

422 The responses of both BU and MerU to F10.7 and ENSO exhibit hemispheric asymmetry. Specifically, the negative
423 (positive) responses of winds to F10.7 are stronger in the SH than those in the NH above the stratospheric polar jet region
424 (around 80 km). The responses of winds to ENSO are positive in the SH stratospheric jet region but are negative in the NH
425 counterpart. Above 80 km, the responses of BU to ENSO are more positive in the SH sub-tropical region than those in NH
426 counterpart. The positive responses of winds to QBO extend to a wider latitude range in the SH stratospheric jet region than
427 those in the NH counterpart. Moreover, the seasonal and linear variations of BU and MerU also exhibit hemispheric
428 asymmetry. Specifically, the peaks of AO of both BU and MerU have larger amplitudes and at lower heights in SH than
429 those in the NH. Although the linear variations of winds depend on the temporal intervals of data, the linear variations are
430 hemispheric asymmetry on aspects of magnitudes and patterns in each temporal interval.

431 Since the regressors are same at all latitudes and heights, the hemispheric asymmetric responses come from the
432 hemispheric asymmetry of zonal winds. Figures 3 and 4 of Liu et al. (2021) have shown that both BU and MerU were faster
433 in the SH than those in the NH, especially when the wind is eastward in winter of each hemisphere. Moreover, the winds at
434 middle and high latitudes of the SH were faster and more stable than those in the NH. One reason is that the SSW occurs
435 frequently (6–7 times per decade) in the NH. During SSW, the eastward wind becomes weak or even reversal (Butler et al.,
436 2015; Baldwin et al., 2021). We note that SSWs in the NH mainly occurred in the phase when the zonal wind was eastward
437 (i.e., the zonal wind was eastward before and after SSWs, while the zonal wind becomes weak or reversed during SSWs). In
438 contrast, the SSW rarely occurred in the SH (only 3 times during 2002–2019, i.e., major SSW in September 2002, minor
439 SSWs in August 2010 and September 2019), mainly due to the weaker land-sea contrast and smaller planetary wave
440 amplitudes in the SH than those in the NH (Eswaraiah et al., 2016; Li et al., 2021; Rao et al., 2020; Butler et al., 2015).

441 The MerU at 60°N/S and 30 km (Fig. 9) show that the SSWs in the NH have influence on the zonal wind at least in the
442 monthly mean sense. However, the influence of SSWs on the zonal wind in the SH is neglectable. If we simply use the zonal
443 wind at 60°N/S and 30 km as a regressor to represent SSW, the prominent responses appear in summer but not in winter
444 (when the SSW occur). This is because SSWs occur only in a limited temporal interval (1–2 weeks) in winter, the zonal wind
445 at 60°N/S and 30 km throughout the temporal interval include both SSWs and other variations. It is desired to develop an
446 index to represent the main features of SSW. This is out of the scope of this work and will be our future work. To illustrate
447 the possible influences of SSWs on BU, we show in Fig. 9 the residuals of BU (BU_{Res}) of Eq. (2) and their absolute values



448 (BU_{Res}) in a composite year. BU_{Res} may represent the effects SSWs on BU to some extent since we did not include SSW as
 449 a regressor in Eq. (2).

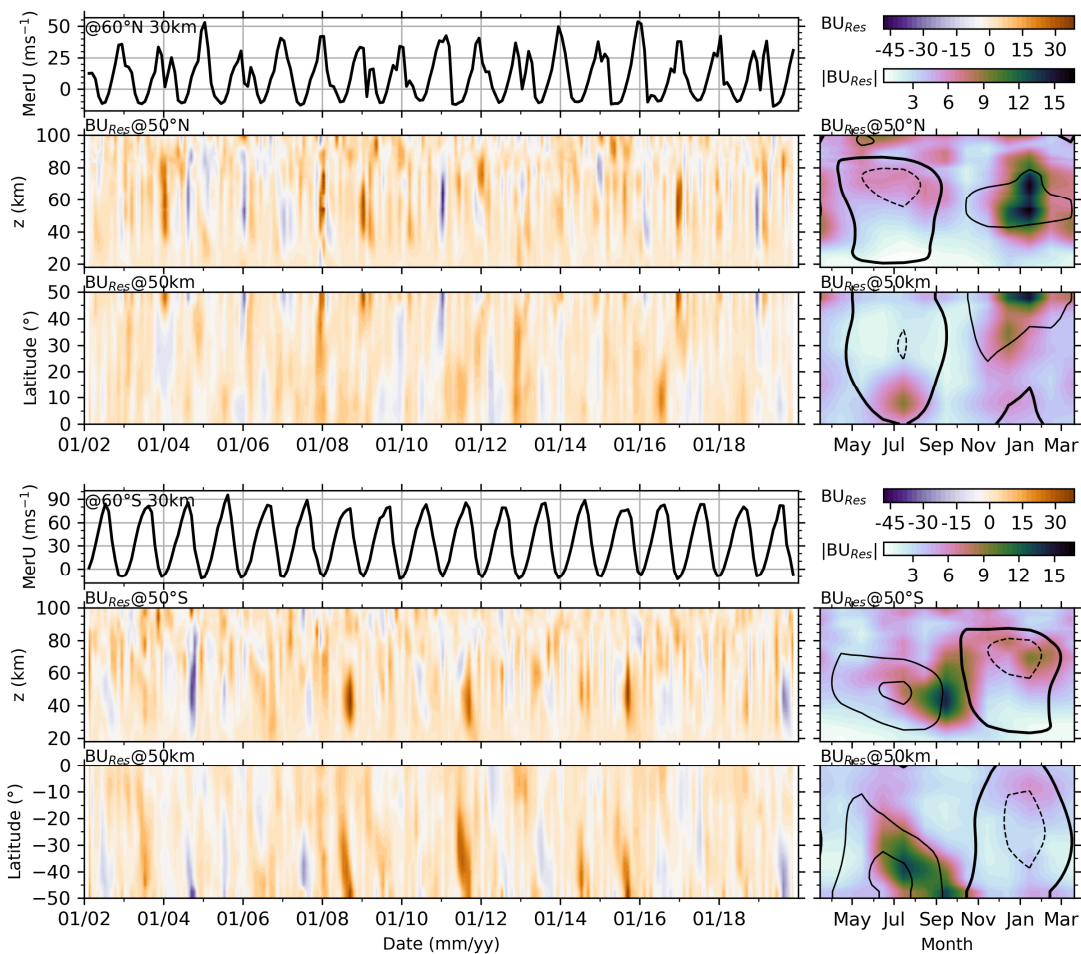


Figure 9: Upper three rows: MerU at 60°N and 30 km (first row) and the residuals of BU (BU_{Res} , the upper color bar in the top-right corner) at 50°N (the second row) and 50 km (the third row), and the absolute values BU_{Res} ($|BU_{Res}|$, the lower color bar in the top-right corner) in a composite year. Lower three rows: same caption as the upper three rows but for the winds in the southern counterpart. The dashed, thick, and solid contour lines indicate the BU of -40, 0, 40 and 80 ms^{-1} , respectively.

450 From Fig. 9, we see that BU_{Res} have larger magnitudes (positive or negative) in the NH when SSWs occur. Meanwhile,



451 the magnitudes of BU_{Res} decrease with the decreasing latitudes. $|BU_{Res}|$ in a composite year has peak around January, when
452 SSWs occur more frequently as revealed from the MerU at 60°N . This indicates that the influences of SSWs on the
453 regression results decrease with the decreasing latitudes in the NH. In contrast, BU_{Res} have larger magnitudes when the zonal
454 winds decelerate from their eastward peaks in the SH. Further examination on the $|BU_{Res}|$ in a composite year, we see that
455 their peaks shift from September at 50°S to July at lower latitudes. The larger $|BU_{Res}|$ is mainly due to the seasonal
456 asymmetry of zonal winds, i.e., the zonal winds take a longer time to reach their eastward peak than that to reach their
457 westward peak.

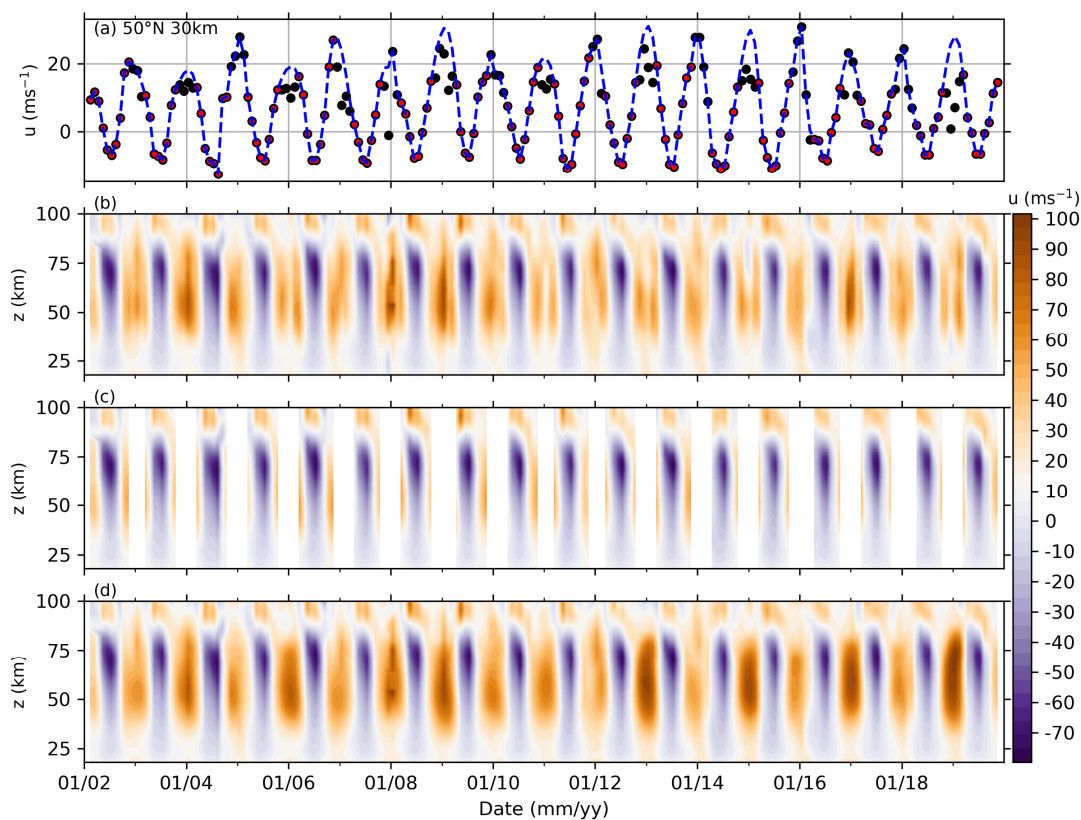


Figure 10: Removing SSWs from the raw BU and the reconstructed BU at 50°N . (a): the remaining data (red dots), which is obtained by removing the data affected by SSWs from raw BU (black dots), and the reconstructed BU (blue dotted line, see text for detail). (b-d): the raw BU, remaining and reconstructed BU, respectively.



458 To test the possible influences of SSWs on the hemispheric asymmetry of the variations and responses, we reconstruct
 459 the BU in the NH during 2002–2019 through the following two steps. First, at each height and latitude, we remove the wind
 460 data during SSWs (i.e., the BU in winter does not increase monotonically before December or decrease monotonically after
 461 December) from the raw wind (shown as black dots in Fig. 10a). Second, cubic spline interpolation is applied on the
 462 remaining data (red dots in Fig. 10a) to get a reconstructed wind series in winter (i.e., it increases monotonically before
 463 December and decreases monotonically after December, shown as blue dashed line in Fig. 10a). Figures 10(b-d) show the
 464 raw BU, remaining and the reconstructed BU, respectively. We see that the decelerated eastward winds during SSWs (Fig.
 465 10b) have been replaced by the reconstructed BU, i.e., the eastward winds accelerate before December and decelerate after
 466 December (Fig. 10d).

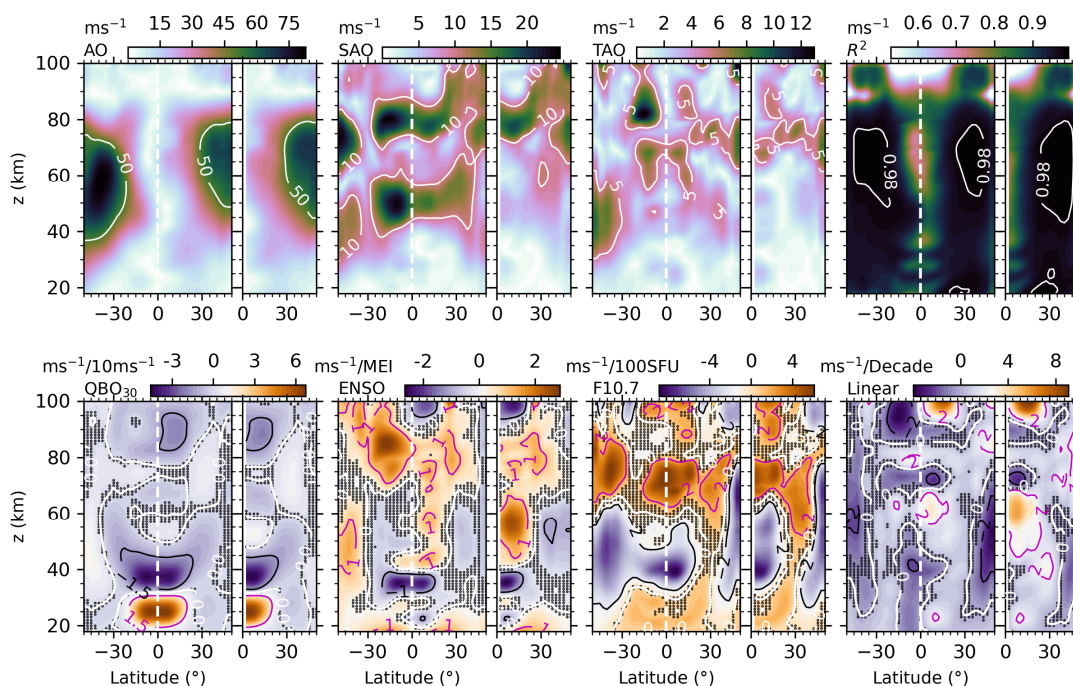


Figure 11: Regression results of the raw (50°S–50°N, left panel of each subplot) and reconstructed BU (0°–50°N, right panel of each subplot) in the NH during 2002–2019. Upper row: same caption as Figure 2. Lower row: same caption as Figure 7.

467 Using Eq. (2), we performed the same regression on the reconstructed winds in the NH. Figure 11 shows the amplitudes
 468 of seasonal variations and R^2 , and the responses of reconstructed winds to QBO, ENSO, F10.7, and the linear variations. For



469 comparison purpose, we also show in Fig. 11 the regression results of the raw BU. The R^2 indicates that Eq. (2) explains the
470 reconstructed winds more accurately than the raw BU in the NH stratospheric polar jet region. The amplitudes of AO of the
471 reconstructed winds are larger than those of the raw BU. However, the amplitudes of SAO and TAO of the reconstructed
472 winds are smaller than those of the raw BU in the NH stratospheric polar jet region. Above 80 km, the amplitudes AO, SAO,
473 TAO of both the reconstructed and raw BUs are nearly identical. The influences of SSWs on the seasonal variations mainly
474 in the stratospheric polar jet region and around ~ 65 km. The influences of QBO₃₀ on the reconstructed winds are similar to
475 those of the raw BU on the aspects of both patterns and magnitudes. The influences of ENSO on the reconstructed winds
476 have similar patterns to those of the raw BU but have larger magnitudes at ~ 55 km. While above ~ 70 km, the influences of
477 ENSO on the reconstructed winds have similar patterns and magnitudes to those of the raw BU. The negative influences of
478 F10.7 on the reconstructed winds extend to ~ 30 – 60 km as compared to the $\sim z=30$ – 50 km for the raw BU in the NH tropical
479 region. The linear variations of the reconstructed winds are more positive at ~ 60 km in the subtropic region but less negative
480 at latitudes higher than 30°N . In a word, compared to the raw BU, the reconstructed wind increases the amplitudes of AO but
481 decreases the amplitudes of SAO and TAO in the NH stratospheric polar jet region. The responses of the reconstructed
482 winds to QBO, ENSO, F10.7, and the linear variations slightly changed on the aspect of magnitudes. However, the
483 hemispheric asymmetry of the responses is not affected by SSWs at least in the monthly mean sense.

484 5 Conclusions

485 A global balance wind dataset (BU) is used to study the variations of the monthly zonal mean winds and responses of
486 the monthly zonal mean winds to solar activity, QBO, ENSO at $\sim z=18$ – 100 km and 50°S – 50°N and from 2002 to 2019. The
487 variations and responses are extracted by MLR method, which is also applied to the MERRA2 zonal wind (MerU) to test the
488 reliability of BU and their responses.

489 The seasonal variations (AO, SAO, and TAO) of BU and MerU have nearly identical phases in the regions where their
490 amplitudes are prominent. Their consistencies are better in the SH than in the NH on the aspects of both patterns and
491 magnitudes. The SAO of BU has peak around 80 km is hemispheric asymmetry and stronger in the SH. The TAO of BU
492 above 80 km is also hemispheric asymmetry and stronger in the SH. The annual mean responses of BU and MerU to F10.7
493 are more negative in the SH stratospheric polar jet region of SH than that of the NH counterpart. Around ~ 80 km, the annual
494 responses of BU to F10.7 are mainly positive in the tropical region. The influences of the stratospheric QBO extend from the
495 equator to higher latitudes with the increasing height. The influences can be positive or negative, which depend on heights
496 and latitudes. Above ~ 80 km, the negative responses of winds to the stratospheric QBO are hemispheric asymmetry and are
497 more negative in the NH tropical regions. Both BU and MerU exhibit similar responses to MEI. Whereas the responses of
498 BU to MEI are stronger than those of MerU at 50°N/S . The responses of winds to MEI propagate downward with the
499 increasing time at 50°N/S and 25°N/S . Both BU and MerU exhibit similar linear variations. The large discrepancy is that the
500 negative variations of BU at 50°N cannot be seen in MerU during October–January. Above 70 km, the patterns of the linear
501 variations of BU are sporadic and strongly dependent on months, latitudes and heights.



502 The robustness of the responses of winds to QBO, ENSO, and F10.7, and the linear variations of winds are examined by
503 changing the temporal interval of the data. We found that the responses of winds to QBO are robust and are almost
504 independent on the temporal intervals. The responses of winds to ENSO are robust but slightly dependent on the temporal
505 intervals. Although the responses of wind to F10.7 have similar patterns in different temporal intervals, the responses are
506 stronger in the temporal intervals of 2002–2015 and 2002–2019 than the other two temporal intervals. The linear variations
507 of both BU and MerU depend strongly on the temporal intervals. The possible reasons might be the different linear
508 variations inhibited in the regressors and (2) the unstable regressors in different temporal intervals. Thus, it is desired to
509 examine the responses and linear variations in different temporal intervals, such that one can get a more comprehensive
510 impression on the linear variations although the exact linear variations are unknown. The influences of SSWs on the seasonal
511 variations are mainly in the NH stratospheric polar jet region. However, the hemispheric asymmetry of the seasonal and
512 linear variations, and the hemispheric asymmetric responses of BU to QBO, ENSO, and F10.7 are not affected by SSWs at
513 least in the monthly mean sense.

514 **Data availability**

515 The global balance wind data can be obtained from National Space Science Data Center
516 (<https://doi.org/10.12176/01.99.00574>) (Last access: March 2022, Liu et al., 2021). The F10.7 data were obtained from
517 <https://spdf.gsfc.nasa.gov/pub/data/omni/> (last access: March 2022, Tapping, 2013). The MERRA2 data were obtained from
518 <http://disc.sci.gsfc.nasa.gov/mdisc> (last access: March 2022, Molod et al., 2015; Gelaro et al., 2017). The QBO data were
519 obtained from <https://www.geo.fu-berlin.de/en/met/ag/strat/produkte/qbo/> (last access: March 2022, Baldwin et al., 2001).
520 The ENSO data were obtained from <https://www.psl.noaa.gov/enso/mei/> (last access: March 2022, Zhang et al., 2019;
521 Wolter and Timlin, 2011).

522 **Author contributions**

523 XL analyzed the data and prepared the paper with assistance from co-authors. JX and JY design the study. All authors
524 reviewed and commented on the paper.

525 **Competing interests**

526 The authors declare that they have no conflict of interest.

527 **Acknowledgments**

528 This work was supported by the National Natural Science Foundation of China (41831073, 42174196, 41874182), the
529 Natural Science Foundation of Henan Province (212300410011), the Project of Stable Support for Youth Team in Basic
530 Research Field, CAS (YSBR-018), the Informatization Plan of Chinese Academy of Sciences (CAS-WX2021PY-0101), and
531 the Open Research Project of Large Research Infrastructures of CAS "Study on the interaction between low/mid-latitude
532 atmosphere and ionosphere based on the Chinese Meridian Project". This work was also supported in part by the Specialized



533 Research Fund and the Open Research Program of the State Key Laboratory of Space Weather.

534 References

- 535 Baldwin, M. P. and O'Sullivan, D.: Stratospheric Effects of ENSO-Related Tropospheric Circulation Anomalies, *J Clim*, 8,
536 649–667, [https://doi.org/10.1175/1520-0442\(1995\)008<0649:SEOERT>2.0.CO;2](https://doi.org/10.1175/1520-0442(1995)008<0649:SEOERT>2.0.CO;2), 1995.
- 537 Baldwin, M. P., Gray, L. J., Dunkerton, T. J., Hamilton, K., Haynes, P. H., Randel, W. J., Holton, J. R., Alexander, M. J.,
538 Hirota, I., Horinouchi, T., Jones, D. B. A., Kinnerson, J. S., Marquardt, C., Sato, K., and Takahashi, M.: The quasi-
539 biennial oscillation, *Reviews of Geophysics*, 39, 179–229, <https://doi.org/10.1029/1999RG000073>, 2001.
- 540 Baldwin, M. P., Ayarzagüena, B., Birner, T., Butchart, N., Butler, A. H., Charlton-Perez, A. J., Domeisen, D. I. V., Garfinkel,
541 C. I., Garny, H., Gerber, E. P., Hegglin, M. I., Langematz, U., and Pedatella, N. M.: Sudden Stratospheric Warmings,
542 <https://doi.org/10.1029/2020RG000708>, 1 March 2021.
- 543 Beig, G., Keckhut, P., Lowe, R. P., Roble, R. G., Mlynczak, M. G., Scheer, J., Fomichev, V. I., Offermann, D., French, W. J.
544 R., Shepherd, M. G., Semenov, A. I., Remsburg, E. E., She, C. Y., Lübken, F. J., Bremer, J., Clemesha, B. R., Stegman,
545 J., Sigernes, F., and Fadnavis, S.: Review of mesospheric temperature trends, *Reviews of Geophysics*, 41,
546 <https://doi.org/10.1029/2002RG000121>, 2003.
- 547 Beig, G., Scheer, J., Mlynczak, M. G., and Keckhut, P.: Overview of the temperature response in the mesosphere and lower
548 thermosphere to solar activity, *Reviews of Geophysics*, 46, <https://doi.org/10.1029/2007RG000236>, 2008.
- 549 Burrage, M. D., Vincent, R. A., Mayr, H. G., Skinner, W. R., Arnold, N. F., and Hays, P. B.: Long-term variability in the
550 equatorial middle atmosphere zonal wind, *Journal of Geophysical Research: Atmospheres*, 101, 12847–12854,
551 <https://doi.org/10.1029/96JD00575>, 1996.
- 552 Butler, A. H., Seidel, D. J., Hardiman, S. C., Butchart, N., Birner, T., and Match, A.: Defining sudden stratospheric
553 warmings, *Bull Am Meteorol Soc*, 96, 1913–1928, <https://doi.org/10.1175/BAMS-D-13-00173.1>, 2015.
- 554 Cai, B., Xu, Q. C., Hu, X., Cheng, X., Yang, J. F., and Li, W.: Analysis of the correlation between horizontal wind and 11-
555 year solar activity over Langfang, China, *Earth and Planetary Physics*, 5, 270–279,
556 <https://doi.org/10.26464/epp2021029>, 2021.
- 557 Coy, L., Wargan, K., Molod, A. M., McCarty, W. R., and Pawson, S.: Structure and dynamics of the Quasi-biennial
558 oscillation in MERRA-2, *J Clim*, 29, 5339–5354, <https://doi.org/10.1175/JCLI-D-15-0809.1>, 2016.
- 559 Domeisen, D. I. V., Garfinkel, C. I., and Butler, A. H.: The Teleconnection of El Niño Southern Oscillation to the
560 Stratosphere, *Reviews of Geophysics*, 57, 5–47, <https://doi.org/10.1029/2018RG000596>, 2019a.
- 561 Domeisen, D. I. V., Garfinkel, C. I., and Butler, A. H.: The Teleconnection of El Niño Southern Oscillation to the
562 Stratosphere, <https://doi.org/10.1029/2018RG000596>, 1 March 2019b.
- 563 Dunkerton, T. J.: Theory of the Mesopause Semiannual Oscillation, *J Atmos Sci*, 39, 2681–2690,
564 [https://doi.org/10.1175/1520-0469\(1982\)039<2681:TOTMSO>2.0.CO;2](https://doi.org/10.1175/1520-0469(1982)039<2681:TOTMSO>2.0.CO;2), 1982.
- 565 Emmert, J. T., Stevens, M. H., Bernath, P. F., Drob, D. P., and Boone, C. D.: Observations of increasing carbon dioxide
566 concentration in Earth's thermosphere, *Nat Geosci*, 5, 868–871, <https://doi.org/10.1038/ngeo1626>, 2012.
- 567 Ern, M., Diallo, M., Preusse, P., Mlynczak, M. G., Schwartz, M. J., Wu, Q., and Riese, M.: The semiannual oscillation (SAO)
568 in the tropical middle atmosphere and its gravity wave driving in reanalyses and satellite observations, *Atmos Chem
569 Phys*, 21, 13763–13795, <https://doi.org/10.5194/acp-21-13763-2021>, 2021.
- 570 Eswarajah, S., Kim, Y. H., Hong, J., Kim, J. H., Ratnam, M. V., Chandran, A., Rao, S. V. B., and Riggan, D.: Mesospheric
571 signatures observed during 2010 minor stratospheric warming at King Sejong Station (62°S, 59°W), *J Atmos Sol Terr
572 Phys*, 140, 55–64, <https://doi.org/10.1016/j.jastp.2016.02.007>, 2016.
- 573 Fleming, E. L., Chandra, S., Barnett, J. J., and Corney, M.: Zonal mean temperature, pressure, zonal wind and geopotential
574 height as functions of latitude, *Advances in Space Research*, 10, 11–59, [https://doi.org/10.1016/0273-1177\(90\)90386-E](https://doi.org/10.1016/0273-1177(90)90386-E),
575 1990.
- 576 Garcia, R. R., Dunkerton, T. J., Lieberman, R. S., and Vincent, R. A.: Climatology of the semiannual oscillation of the
577 tropical middle atmosphere, *Journal of Geophysical Research Atmospheres*, 102, <https://doi.org/10.1029/97jd00207>,
578 1997.



- 579 Garcia, R. R., Yue, J., and Russell, J. M.: Middle Atmosphere Temperature Trends in the Twentieth and Twenty-First
580 Centuries Simulated With the Whole Atmosphere Community Climate Model (WACCM), *J Geophys Res Space Phys*,
581 124, 7984–7993, <https://doi.org/10.1029/2019JA026909>, 2019.
- 582 Gelaro, R., McCarty, W., Suárez, M. J., Todling, R., Molod, A., Takacs, L., Randles, C. A., Darmenov, A., Bosilovich, M.
583 G., Reichle, R., Wargan, K., Coy, L., Cullather, R., Draper, C., Akella, S., Buchard, V., Conaty, A., da Silva, A. M., Gu,
584 W., Kim, G. K., Koster, R., Lucchesi, R., Merkova, D., Nielsen, J. E., Partyka, G., Pawson, S., Putman, W., Rienecker,
585 M., Schubert, S. D., Sienkiewicz, M., and Zhao, B.: The modern-era retrospective analysis for research and applications,
586 version 2 (MERRA-2), *J Clim*, 30, 5419–5454, <https://doi.org/10.1175/JCLI-D-16-0758.1>, 2017.
- 587 Hayashi, H., Koyama, Y., Hori, T., Tanaka, Y., Abe, S., Shinbori, A., Kagitani, M., Kouno, T., Yoshida, D., UeNo, S.,
588 Kaneda, N., Yoneda, M., Umemura, N., Tadokoro, H., and Motoba, T.: Inter-university upper atmosphere global
589 observation network (IUGONET), *Data Sci J*, 12, 179–184, <https://doi.org/10.2481/dsj.WDS-030>, 2013.
- 590 Keuer, D., Hoffmann, P., Singer, W., and Bremer, J.: Long-term variations of the mesospheric wind field at mid-latitudes,
591 *Ann Geophys*, 25, 1779–1790, <https://doi.org/10.5194/angeo-25-1779-2007>, 2007.
- 592 Kumar, K. K.: Is Mesospheric Quasi Biennial Oscillation Ephemeral?, <https://doi.org/10.1029/2020GL091033>, 28 January
593 2021.
- 594 Kutner, M., Neter, C. N. J., and Li, W.: *Applied Linear Statistical Models*, 5th ed., McGraw-Hill Irwin, Boston, 258 pp.,
595 2004.
- 596 Laštovička, J.: A review of recent progress in trends in the upper atmosphere, *J Atmos Sol Terr Phys*, 163, 2–13,
597 <https://doi.org/10.1016/j.jastp.2017.03.009>, 2017.
- 598 Li, N., Lei, J., Huang, F., Yi, W., Chen, J., Xue, X., Gu, S., Luan, X., Zhong, J., Liu, F., Dou, X., Qin, Y., and Owolabi, C.:
599 Responses of the Ionosphere and Neutral Winds in the Mesosphere and Lower Thermosphere in the Asian-Australian
600 Sector to the 2019 Southern Hemisphere Sudden Stratospheric Warming, *J Geophys Res Space Phys*, 126,
601 <https://doi.org/10.1029/2020JA028653>, 2021.
- 602 Li, T., Leblanc, T., McDermaid, I. S., Keckhut, P., Hauchecorne, A., and Dou, X.: Middle atmosphere temperature trend and
603 solar cycle revealed by long-term Rayleigh lidar observations, *Journal of Geophysical Research Atmospheres*, 116, 1–
604 11, <https://doi.org/10.1029/2010JD015275>, 2011.
- 605 Li, T., Liu, A. Z., Lu, X., Li, Z., Franke, S. J., Swenson, G. R., and Dou, X.: Meteor-radar observed mesospheric semi-
606 annual oscillation (SAO) and quasi-biennial oscillation (QBO) over Maui, Hawaii, *Journal of Geophysical Research*
607 *Atmospheres*, 117, <https://doi.org/10.1029/2011JD016123>, 2012.
- 608 Li, T., Calvo, N., Yue, J., Dou, X., Russell, J. M., Mlynczak, M. G., She, C. Y., and Xue, X.: Influence of El Niño-Southern
609 oscillation in the mesosphere, *Geophys Res Lett*, 40, 3292–3296, <https://doi.org/10.1002/grl.50598>, 2013.
- 610 Li, T., Calvo, N., Yue, J., Russell, J. M., Smith, A. K., Mlynczak, M. G., Chandran, A., Dou, X., and Liu, A. Z.: Southern
611 Hemisphere summer mesopause responses to El Niño-Southern Oscillation, *J Clim*, 29, 6319–6328,
612 <https://doi.org/10.1175/JCLI-D-15-0816.1>, 2016.
- 613 Lin, J. and Qian, T.: Impacts of the ENSO Lifecycle on Stratospheric Ozone and Temperature, *Geophys Res Lett*, 46,
614 10646–10658, <https://doi.org/10.1029/2019GL083697>, 2019.
- 615 Liu, X., Yue, J., Xu, J., Garcia, R. R., Russell, J. M., Mlynczak, M., Wu, D. L., and Nakamura, T.: Variations of global
616 gravity waves derived from 14 years of SABER temperature observations, *J Geophys Res*, 122, 6231–6249,
617 <https://doi.org/10.1002/2017JD026604>, 2017.
- 618 Liu, X., Xu, J., Yue, J., Yu, Y., Batista, P. P., Andrioli, V. F., Liu, Z., Yuan, T., Wang, C., Zou, Z., Li, G., and Russell III, J.
619 M.: Global balanced wind derived from SABER temperature and pressure observations and its validations, *Earth Syst*
620 *Sci Data*, 13, 5643–5661, <https://doi.org/10.5194/essd-13-5643-2021>, 2021.
- 621 Liu, X., Xu, J., Yue, J., and Kogure, M.: Persistent Layers of Enhanced Gravity Wave Dissipation in the Upper Mesosphere
622 Revealed From SABER Observations, *Geophys Res Lett*, 49, <https://doi.org/10.1029/2021GL097038>, 2022.
- 623 Lübken, F. J., Berger, U., and Baumgarten, G.: On the Anthropogenic Impact on Long-Term Evolution of Noctilucent
624 Clouds, *Geophys Res Lett*, 45, 6681–6689, <https://doi.org/10.1029/2018GL077719>, 2018.
- 625 Manney, G. L. and Hegglin, M. I.: Seasonal and Regional Variations of Long-Term Changes in Upper-Tropospheric Jets
626 from Reanalyses, *J Clim*, 31, 423–448, <https://doi.org/10.1175/JCLI-D-17-0303.1>, 2018.



- 627 Manzini, E., Giorgetta, M. A., Esch, M., Kornblueh, L., and Roeckner, E.: The Influence of Sea Surface Temperatures on the
628 Northern Winter Stratosphere: Ensemble Simulations with the MAECHAM5 Model, *J Clim*, 19, 3863–3881,
629 <https://doi.org/10.1175/JCLI3826.1>, 2006.
- 630 Matsumoto, N., Shinbori, A., Riggin, D., and Tsuda, T.: Measurement of momentum flux using two meteor radars in
631 Indonesia. *Ann Geophys*, 34, 369–377, <https://doi.org/10.5194/angeo-34-369-2016>, 2016.
- 632 Mlynczak, M. G., Hunt, L. A., Garcia, R. R., Harvey, V. L., Marshall, B. T., Yue, J., Mertens, C. J., and Russell, J. M.:
633 Cooling and Contraction of the Mesosphere and Lower Thermosphere From 2002 to 2021, *Journal of Geophysical*
634 *Research: Atmospheres*, 127, <https://doi.org/10.1029/2022JD036767>, 2022.
- 635 Molod, A., Takacs, L., Suarez, M., and Bacmeister, J.: Development of the GEOS-5 atmospheric general circulation model:
636 Evolution from MERRA to MERRA2, *Geosci Model Dev*, 8, 1339–1356, <https://doi.org/10.5194/gmd-8-1339-2015>,
637 2015.
- 638 Mudelsee, M.: Trend analysis of climate time series: A review of methods, <https://doi.org/10.1016/j.earscirev.2018.12.005>, 1
639 March 2019.
- 640 Polvani, L. M. and Waugh, D. W.: Upward Wave Activity Flux as a Precursor to Extreme Stratospheric Events and
641 Subsequent Anomalous Surface Weather Regimes, *J Clim*, 17, 3548–3554, [https://doi.org/10.1175/1520-0442\(2004\)017<3548:UWAFAA>2.0.CO;2](https://doi.org/10.1175/1520-0442(2004)017<3548:UWAFAA>2.0.CO;2), 2004.
- 642 Qian, L., Jacobi, C., and McInerney, J.: Trends and Solar Irradiance Effects in the Mesosphere, *J Geophys Res Space Phys*,
643 124, 1343–1360, <https://doi.org/10.1029/2018JA026367>, 2019.
- 644 Ramesh, K., Smith, A. K., Garcia, R. R., Marsh, D. R., Sridharan, S., and Kishore Kumar, K.: Long-Term Variability and
645 Tendencies in Middle Atmosphere Temperature and Zonal Wind From WACCM6 Simulations During 1850–2014,
646 *Journal of Geophysical Research: Atmospheres*, 125, <https://doi.org/10.1029/2020JD033579>, 2020.
- 647 Randel, W. J.: The Evaluation of Winds from Geopotential Height Data in the Stratosphere, *J Atmos Sci*, 44, 3097–3120,
648 [https://doi.org/10.1175/1520-0469\(1987\)044<3097:TEOWFG>2.0.CO;2](https://doi.org/10.1175/1520-0469(1987)044<3097:TEOWFG>2.0.CO;2), 1987.
- 649 Randel, W. J. and Cobb, J. B.: Coherent variations of monthly mean total ozone and lower stratospheric temperature, *J*
650 *Geophys Res*, 99, 5433, <https://doi.org/10.1029/93JD03454>, 1994.
- 651 Randel, W. J., Udelhofen, P., Fleming, E., Geller, M., Gelman, M., Hamilton, K., Karoly, D., Ortland, D., Pawson, S.,
652 Swinbank, R., Wu, F., Baldwin, M., Chanin, M.-L., Keckhut, P., Labitzke, K., Remsberg, E., Simmons, A., and Wu, D.:
653 The SPARC Intercomparison of Middle-Atmosphere Climatologies, *J Clim*, 17, 986–1003,
654 [https://doi.org/10.1175/1520-0442\(2004\)017<0986:TSIOMC>2.0.CO;2](https://doi.org/10.1175/1520-0442(2004)017<0986:TSIOMC>2.0.CO;2), 2004.
- 655 Randel, W. J., Garcia, R. R., Calvo, N., and Marsh, D.: ENSO influence on zonal mean temperature and ozone in the tropical
656 lower stratosphere, *Geophys Res Lett*, 36, <https://doi.org/10.1029/2009GL039343>, 2009.
- 657 Randel, W. J., Polvani, L., Wu, F., Kinnison, D. E., Zou, C. Z., and Mears, C.: Troposphere-Stratosphere Temperature
658 Trends Derived From Satellite Data Compared With Ensemble Simulations From WACCM, *Journal of Geophysical*
659 *Research: Atmospheres*, 122, 9651–9667, <https://doi.org/10.1002/2017JD027158>, 2017.
- 660 Rao, J., Garfinkel, C. I., White, I. P., and Schwartz, C.: The Southern Hemisphere Minor Sudden Stratospheric Warming in
661 September 2019 and its Predictions in S2S Models, *Journal of Geophysical Research: Atmospheres*, 125,
662 <https://doi.org/10.1029/2020JD032723>, 2020.
- 663 Ray, E. A., Alexander, M. J., and Holton, J. R.: An analysis of the structure and forcing of the equatorial semiannual
664 oscillation in zonal wind, *Journal of Geophysical Research Atmospheres*, 103, 1759–1774,
665 <https://doi.org/10.1029/97JD02679>, 1998.
- 666 Russell III, J. M., Mlynczak, M. G., Gordley, L. L., Tansock, Jr., J. J., and Esplin, R. W.: Overview of the SABER
667 experiment and preliminary calibration results, in: *Optical Spectroscopic Techniques and Instrumentation for*
668 *Atmospheric and Space Research III*, 277–288, <https://doi.org/10.1117/12.366382>, 1999.
- 669 She, C. Y., Berger, U., Yan, Z. A., Yuan, T., Lübken, F. J., Krueger, D. A., and Hu, X.: Solar Response and Long-Term
670 Trend of Midlatitude Mesopause Region Temperature Based on 28 Years (1990–2017) of Na Lidar Observations, *J*
671 *Geophys Res Space Phys*, 124, 7140–7156, <https://doi.org/10.1029/2019JA026759>, 2019.
- 672 Smith, A. K., Garcia, R. R., Moss, A. C., and Mitchell, N. J.: The semiannual oscillation of the tropical zonal wind in the
673 middle atmosphere derived from satellite geopotential height retrievals, *J Atmos Sci*, 74, 2413–2425,
674 <https://doi.org/10.1175/JAS-D-17-0067.1>, 2017.
- 675



- 676 Souleymane, S. Y., Madonna, F., Rosoldi, M., Tramutola, E., Gagliardi, S., Proto, M., and Pappalardo, G.: Sensitivity of
677 trends to estimation methods and quantification of subsampling effects in global radiosounding temperature and
678 humidity time series, *International Journal of Climatology*, 41, E1992–E2014, <https://doi.org/10.1002/joc.6827>, 2021.
- 679 Sridharan, S., Tsuda, T., and Gurubaran, S.: Radar observations of long-term variability of mesosphere and lower
680 thermosphere winds over Tirunelveli (8.7°N, 77.8°E), *Journal of Geophysical Research Atmospheres*, 112,
681 <https://doi.org/10.1029/2007JD008669>, 2007.
- 682 Taguchi, M.: Observed connection of the stratospheric quasi-biennial oscillation with El Niño–Southern Oscillation in
683 radiosonde data, *Journal of Geophysical Research Atmospheres*, 115, <https://doi.org/10.1029/2010JD014325>, 2010.
- 684 Tapping, K. F.: The 10.7 cm solar radio flux (F10.7), *Space Weather*, 11, 394–406, <https://doi.org/10.1002/swe.20064>, 2013.
- 685 Venkat Ratnam, M., Kumar, G. K., Venkateswara Rao, N., Murthy, B. V. K., Laštovička, J., and Qian, L.: Evidence of long-
686 term change in zonal wind in the tropical lower mesosphere: Observations and model simulations, *Geophys Res Lett*,
687 40, 397–401, <https://doi.org/10.1002/grl.50158>, 2013.
- 688 Venkat Ratnam, M., Akhil Raj, S. T., and Qian, L.: Long-Term Trends in the Low-Latitude Middle Atmosphere
689 Temperature and Winds: Observations and WACCM-X Model Simulations, *J Geophys Res Space Phys*, 124, 7320–
690 7331, <https://doi.org/10.1029/2019JA026928>, 2019.
- 691 Venkateswara Rao, N., Tsuda, T., Rigglin, D. M., Gurubaran, S., Reid, I. M., and Vincent, R. A.: Long-term variability of
692 mean winds in the mesosphere and lower thermosphere at low latitudes, *J Geophys Res Space Phys*, 117, 1–16,
693 <https://doi.org/10.1029/2012JA017850>, 2012.
- 694 Wolter, K. and Timlin, M. S.: El Niño/Southern Oscillation behaviour since 1871 as diagnosed in an extended multivariate
695 ENSO index (MEI.ext), *International Journal of Climatology*, 31, 1074–1087, <https://doi.org/10.1002/joc.2336>, 2011.
- 696 Xu, J., Smith, A. K., Yuan, W., Liu, H.-L., Wu, Q., Mlynczak, M. G., and Russell, I. M.: Global structure and long-term
697 variations of zonal mean temperature observed by TIMED/SABER, *Journal of Geophysical Research Atmospheres*, 112,
698 1–20, <https://doi.org/10.1029/2007JD008546>, 2007.
- 699 Xu, J., Smith, A. K., Liu, H. L., Yuan, W., Wu, Q., Jiang, G., Mlynczak, M. G., and Russell, J. M.: Estimation of the
700 equivalent Rayleigh friction in mesosphere/lower thermosphere region from the migrating diurnal tides observed by
701 TIMED, *Journal of Geophysical Research Atmospheres*, 114, 1–20, <https://doi.org/10.1029/2009JD012209>, 2009a.
- 702 Xu, J., Smith, A. K., Liu, H. L., Yuan, W., Wu, Q., Jiang, G., Mlynczak, M. G., Russell, J. M., and Franke, S. J.: Seasonal
703 and quasi-biennial variations in the migrating diurnal tide observed by Thermosphere, Ionosphere, Mesosphere,
704 Energetics and Dynamics (TIMED), *Journal of Geophysical Research Atmospheres*, 114, 1–16,
705 <https://doi.org/10.1029/2008jd011298>, 2009b.
- 706 Yuan, T., Solomon, S. C., She, C. Y., Krueger, D. A., and Liu, H. L.: The Long-Term Trends of Nocturnal Mesopause
707 Temperature and Altitude Revealed by Na Lidar Observations Between 1990 and 2018 at Midlatitude, *Journal of*
708 *Geophysical Research: Atmospheres*, 124, 5970–5980, <https://doi.org/10.1029/2018JD029828>, 2019.
- 709 Yue, J., Russell, J., Jian, Y., Rezac, L., Garcia, R., López-Puertas, M., and Mlynczak, M. G.: Increasing carbon dioxide
710 concentration in the upper atmosphere observed by SABER, *Geophys Res Lett*, 42, 7194–7199,
711 <https://doi.org/10.1002/2015GL064696>, 2015.
- 712 Yue, J., Russell, J., Gan, Q., Wang, T., Rong, P., Garcia, R., and Mlynczak, M.: Increasing Water Vapor in the Stratosphere
713 and Mesosphere After 2002, *Geophys Res Lett*, 46, 13452–13460, <https://doi.org/10.1029/2019GL084973>, 2019a.
- 714 Yue, J., Li, T., Qian, L., Lastovička, J., and Zhang, S.: Introduction to Special Issue on “Long-Term Changes and Trends in
715 the Middle and Upper Atmosphere,” *J Geophys Res Space Phys*, 124, 10360–10364,
716 <https://doi.org/10.1029/2019JA027462>, 2019b.
- 717 Zhang, T., Hoell, A., Perlwitz, J., Eischeid, J., Murray, D., Hoerling, M., and Hamill, T. M.: Towards Probabilistic
718 Multivariate ENSO Monitoring, *Geophys Res Lett*, 46, 10532–10540, <https://doi.org/10.1029/2019GL083946>, 2019.
- 719